JOURNAL OF STRUCTURAL BIOLOGY **119,** 172–188 (1997)
ARTICLE NO. SB973875

Adsorption of Biological Molecules to a Solid Support for Scanning Probe Microscopy

Daniel J. Müller

M.E. Müller-Institute for Microscopy, Biozentrum, University of Basel, Klingelbergstrasse 70, CH-4056 Basel, Switzerland; and IBI-2: Structural Biology, Forschungszentrum Jülich, D-52425 Jülich, Germany

Mattihas Amrein

Institut für Medizinische Physik und Biophysik, Universität Münster, Robert-Koch-Strasse 31, D-48149 Münster, Germany

and

Andreas Engel

M.E. Müller-Institute for Microscopy, Biozentrum, University of Basel, Klingelbergstrasse 70, CH-4056 Basel, Switzerland

Received February 14, 1997

Scanning probe microscopes are now established tools to study the surface structure of biological macromolecules under physiological conditions. Sample preparation methods for this microscopy all have the objective to attach the specimen firmly to a support. Here we analyze the commonly used method of adsorbing biological specimens to freshly cleaved mica. This is facilitated by adjusting the electrolyte concentration and the pH of the buffer solution. Native macromolecular systems adsorbed to mica in this way can be reproducibly imaged at submolecular resolution. © 1997 Academic Press

INTRODUCTION

Scanning probe microscopes (SPM) represent a growing family of microscopes, all of which are closely related to the first instrument of this kind, the scanning tunneling microscope (STM; Binnig *et al.*, 1982). They have in common that an atomically sharp probe is scanned in close proximity to the sample surface, exploiting different interactions between the probe and the sample to acquire atomic scale structural information on the sample surface. One key advantage of such microscopes for biological applications is their ability to image samples in aqueous environments (Drake *et al.*, 1989). With the atomic force microscope (AFM; Binnig *et al.*, 1986) it is not only possible to depict native biomolecules at subnanometer resolution (for a recent review see Engel *et al.*, 1997), but also to directly monitor reversible structural changes of single proteins (Müller *et al.*, 1995a, 1996a, 1997a). In many SPM modes, lateral forces are exerted by the scanning tip on the sample. Thus, a firm attachment of the biological macromolecule to the supporting surface is required to achieve high resolution.

To this end, specimens may be covalently linked to a chemically modified support (Karrasch *et al.*, 1993; Hegner *et al.*, 1993, 1996; Wagner *et al.*, 1994, 1995). Most of the time, however, physisorption is sufficient. The specimens can be directly adsorbed from a physiological buffer solution and any covalent modification, potentially hazardous to the biomolecule, is avoided. The relevant forces that drive the physisorption process are the van der Waals force, the electrostatic double-layer force (EDL force), as well as the hydrophobic effect. Unlike the van der Waals interaction, the EDL force depends strongly on the concentration and valency of charged solutes, as well as the surface charge density of both support and specimen. The EDL force between two equally charged surfaces is repulsive and hence opposite to the van der Waals attraction. Supramolecular structures become attached to a support (for example, mica, gold, silicon, glass) when there is a net attractive force between them and the support pulling their surfaces into contact. Once the molecules are bound, specific interactions like hydrogen bonds or salt bridges can arise.

In this work we demonstrate both experimentally and theoretically how the adsorption of a sample to

1047-8477/97 $25.00
Copyright © 1997 by Academic Press
All rights of reproduction in any form reserved.

freshly cleaved mica can be manipulated by adjusting the ion content and the pH of the buffer solution. As an example, the interaction force between purple membrane and mica is calculated as a function of the electrolyte content using the Derjaguin, Landau, Verwey, Overbeek (DLVO) theory (Israelachvili, 1991). Experimental results show that the membranes adsorb to the mica when the double-layer repulsion is smaller than the attractive van der Waals force for all distances between specimen and support. A similar phenomenon has been reported by Butt (1991), who observed that a silicon nitride tip is attracted by freshly cleaved mica at sufficiently high electrolyte concentrations. We have also selected mica as it is the most commonly used support for imaging biological specimens with the AFM. Purple membrane is a well-characterized test specimen (Lanyi, 1993) with known surface charge density (Butt, 1992b), allowing experimental and theoretical results to be compared quantitatively. The general applicability of the described technique is demonstrated with a variety of lipidic and proteinous specimens.

MATERIALS AND METHODS

General Procedure for Adsorption

Freshly cleaved mica (Mica New York Corp., 75 Varick Street, N.Y. 10013) was coated with 25 µl of buffer solution that contained the biological specimen at a concentration of typically 1–20 µg/ml at room temperature. After an adsorption period the mica was washed gently to remove molecules that were not firmly attached. All buffer solutions were prepared from ultrapure water (fresh mili-Q water; ≤18 MΩ/cm) and grade p.a. chemicals from Sigma, 9470 Buchs, Switzerland or E. Merck, 8029 Zürich, Switzerland. Solutions were all prepared shortly before the experiments. Citric acid (pH 3–6), 2-(*N*-morpholino)ethanesulfonic acid (Mes; pH 6–7), *N*-2-hydroxylethylpiperazine-*N'*-2-ethanesulfonic acid (Hepes; pH 7–8), and Tris(hydroxylmethyl)aminomethane (Tris; pH 8–10) were used as buffers.

Biological Specimens

Amylin protofilaments. Synthetic human amylin (Bachem California, Torrance, CA) was diluted in ultrapure water in 50 m*M* Tris–HCl at pH 7.6 to a concentration of 1 mg/ml. The peptide solution was then diluted to a concentration of about 50 µg/ml in the adsorption buffer and deposited on the mica. After 10 min the sample was washed with the adsorption buffer to remove loosely attached amylin.

Aquaporin-1. Aquaporin-1 (AQP1) from human erythrocytes was reconstituted into two-dimensional (2D) crystalline sheets in the presence of *Escherichia coli* phospholipids (Walz *et al.*, 1994). The 2D crystals were diluted in the adsorption buffer to a concentration of about 5 µg/ml and deposited on the mica. After 1 hr the sample was washed with buffer prior to imaging by AFM.

Hexagonally packed intermediate layer. HPI layer was extracted from whole cells (strain SARK) with sodium dodecyl sulfate and purified on a Percoll density gradient (Baumeister *et al.*, 1982). A stock solution (1 mg/ml protein) in distilled water was diluted to 20 µg/ml in the adsorption buffer and was deposited on the freshly cleaved mica. After an adsorption time of 1 hr the sample was gently washed with adsorption buffer.

Liposomes. A tetraether lipid fraction was isolated from *Sulfolobus acidocaldarius* (Elferink *et al.*, 1993). The lipids formed closed, stable unilamelar liposomes in aqueous solution. Large unilamellar liposomes with mean diameter of 220 nm (Elferink *et al.*, 1994) were prepared by freeze-thawing a solution containing the lipids (10 mg/ml) five times, followed by extrusion through a Lipofast 200-nm filter. The sample (10 mg/ml (lipid); 100 m*M* potassium phosphate, pH 7, 0.02% azide) was diluted 200-fold in buffer and deposited (20 µl) onto freshly cleaved mica. After 1 hr the sample was ready to be imaged by AFM.

Porin OmpF. Porin OmpF trimers (1 mg/ml) from *E. coli* B^e strain BZB111 (Hoenger *et al.*, 1993) were reconstituted in a temperature-controlled dialysis device (Jap *et al.*, 1992). The solution containing 1 mg protein/ml was diluted 100-fold in the adsorption buffer and deposited onto freshly cleaved mica. After 2 hr the sample was gently washed and imaged by AFM.

Photosystem II. Native photosystem II cores from spinach were extracted with octylthioglucoside and isolated as described (Mishra and Ghanotakis, 1994). The protein solution was diluted in adsorption buffer to a concentration of about 5 µg/ml and deposited on mica. After an adsorption time of 24 hr at 4°C the sample was imaged by AFM.

Phosphatidylethanolamine. 1,2-Dipalmitoyl phosphatidylethanolamine (DPPE) was solubilized in chloroform:hexane (1:1) to a concentration of 1 mg/ml. After this solution was diluted 20-fold in adsorption buffer a drop was deposited on freshly cleaved mica and the sample was allowed to adsorb for 5–15 min.

Purple membrane. Purple membrane of *Halobacterium salinarium* strain ET1001 was isolated as described by Oesterhelt and Stoeckenius (1974). The membranes were frozen and stored at −70°C. Thawed samples were kept at 4°C. A stock solution (10 mg/ml protein) in distilled water was diluted to 10 or 40 µg/ml (for measuring adsorption density) in adsorption buffer prior to adsorption to freshly cleaved mica. After an adsorption time of 5 min the sample was washed in the same buffer and imaged.

Ø29 connector. The Ø29 connectors were overexpressed in *E. coli* carrying a recombinant plasmid with the connector protein gene *p10*. The assembled connector was purified according to Ibañez *et al.* (1984). To obtain two-dimensional crystals, the ionic strength of the protein solution (3 to 4 mg/ml protein) was increased to 2 *M* NaCl at 4°C (Valpuesta *et al.*, 1994). After a few hours the connectors formed crystals a few micrometers in diameter. Prior to adsorption the crystals were diluted to a concentration of about 1 µg/ml. After an adsorption time of 0.5 to 1 hr the sample was gently washed with buffer prior to imaging with the AFM.

Instrumentation and Operation of the AFM

All images were recorded in contact made with a commercial AFM (Nanoscope III, Digital Instruments, Santa Barbara, CA 93117) equipped with a 15-µm scanner (d-scanner) or a 120-µm scanner (j-scanner). Before use, the AFM liquid cell was washed for 10 min in an ultrasonic (50 kHz) bath with ethanol, then sonicated for 10 min in ultrapure water, and allowed to dry in a stream of N_2. Cantilevers, equipped with oxide sharpened silicon nitride tips, were 120 or 200 µm long and had nominal force constants of 0.38 and 0.06 N/m, respectively (Digital Instruments). The samples were mounted in two different ways, to which both proved equally well suited. In one, mica discs (diameter, 6 mm) were glued onto a Teflon disc (diameter, 14 mm) by water-insoluble epoxy (Araldit, Ciba-Geigy, Basel, Switzerland). These teflon discs were glued to steel discs and then mounted on to the piezoelectric scanner. Alternatively, a mica disc (diameter, 14

mm) was directly glued to the steel disc (diameter, 12 mm). Because the buffer solution had contact only with freshly cleaved mica and the quartz glass of the liquid cell, no O-ring seal was required. After thermal relaxation of the microscope, the drift of the cantilever deflection angle corresponded to approximately 0.3 nm per minute. The applied force was corrected manually to compensate for this drift during scanning.

At low magnification (frame size larger than 600 nm) imaging was performed in the error signal mode, acquiring the deflection and height signals simultaneously. The error signal was minimized by optimizing the feedback gain and scan speed. The scan speed was roughly linear to the scan size, 4 to 8 lines per second for lower magnifications (frame size 0.35 to 13 μm) and 8 to 9.6 lines per second for higher magnifications (frame sizes 80 to 130 nm). Hence, the maximum scan speed (1.25 μm/sec) was below the critical value for high-resolution imaging (2 μm/sec; Butt *et al.*, 1993). At high magnification, the deformation of the sample was monitored by comparing the height profiles acquired in the trace and retrace directions and at different scan angles.

Height calibration of the scanner was carried out using layered crystals such as transition metal dichalcogenides (Wilson and Yoffe, 1969) as standards (Müller and Engel, 1997c). The lateral calibration was carried out using purple membrane (Müller *et al.*, 1995b).

Theoretical Considerations

The DLVO theory allows the forces between the purple membrane and the supporting mica to be described quantitatively. Van der Waals (F_{vdW}) forces and the electrostatic double-layer force (F_{el}) are considered, while other interactions are neglected. According to the Lifshitz theory the van der Waals force per unit area between two flat surfaces is given as (Israelachvili, 1991)

$$F_{vdW}(z) = \frac{-H_a}{6\pi z^3}, \qquad (1)$$

where z is the separation of the two surfaces. H_a, the Hamaker constant, characterizes the interaction of the two surfaces (media) across a third medium. For example, for hydrocarbons in water the Hamaker constant is about $0.2–1 \times 10^{-20}$ J (Butt *et al.*, 1995) and for two silicon oxide surfaces in water 8.3×10^{-21} J (Israelachvili, 1991). Solid surfaces in aqueous solutions are charged. This surface charge is balanced by bound counter ions

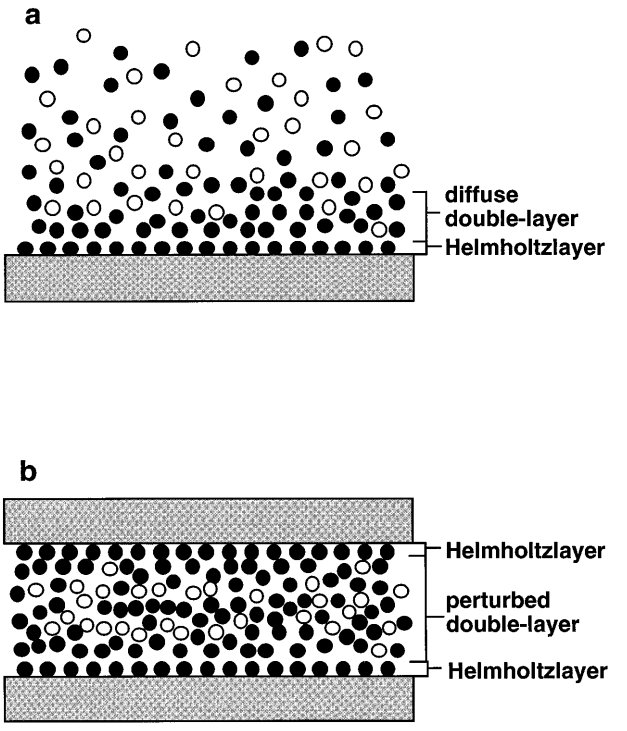

FIG. 1. Specific interaction of ions at solid–liquid interfaces. (a) As result of the Coulomb forces between surface charges and electrolytes and diffusion, a layer of firmly bound ions (Helmholtz or Stern layer) and a diffuse charge cloud form at the solid surface the electric double layer. (b) Two equally charged surfaces at a separation $<\lambda_D$. The ion clouds of the electrical double layer overlap to produce an increase in the osmotic pressure resulting in a repulsive force.

that form the Helmholtz layer and a thin diffuse charge cloud resulting from electrostatic attraction and thermal diffusion (Fig. 1a). This diffuse electric double layer gives rise to repulsive forces between equally charged surfaces.

When two surfaces approach one another their electrical double

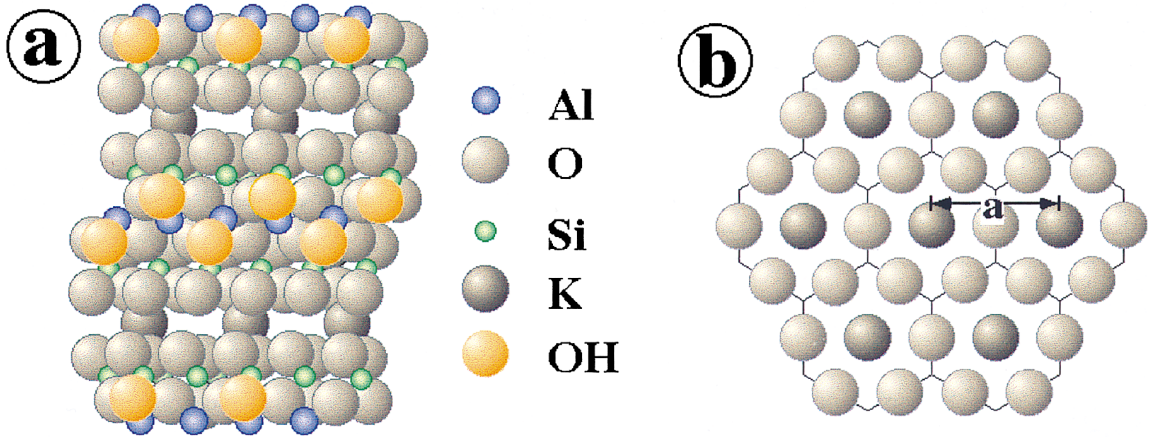

FIG. 2. Structure of muscovite mica. (a) Schematic view along the y axis. Tetrahedral double sheets of $(Si, Al)_2O_5$ are electrostatically linked by potassium ions. At the central Al ions the displacement of the sheets is determined to be $a/3$. The repeat distance perpendicular to the sheets is 10 Å. (b) The basal plane (0001) of mica and the layer of cations (a = 5.2 Å; Bailey, 1984).

layers begin to overlap (Fig. 1b), resulting in an increase of the osmotic pressure and therefore in the double-layer force F_{el}. For most biological systems the surface potentials are small ($|\psi_0| < 25$ mV), and the electrostatic force per unit area of two ultrasmooth, planar surfaces (e.g., mica and purple membrane) can be written as (Israelachvili, 1991)

$$F_{el}(z) = \frac{2\sigma_s\sigma_p}{\epsilon_e\epsilon_0} e^{-z/\lambda_D}, \qquad (2)$$

where λ_D is the Debye length, ϵ_0 the vacuum dielectric permittivity, ϵ_e the dielectric permittivity of the electrolyte, and σ_s and σ_p represent the surface charge densities of the support and the sample, respectively. The Debye length at 25°C, which represents the thickness of the EDL, depends on the valency and the concentration e_c of the electrolyte (Israelachvili, 1991):

$$\lambda_D = \frac{0.304}{\sqrt{e_c}} \text{ nm}$$

for monovalent electrolytes

$$= \frac{0.174}{\sqrt{e_c}} \text{ nm}$$

for divalent (1:2 or 2:1) electrolytes

$$= \frac{0.152}{\sqrt{e_c}} \text{ nm} \qquad (3)$$

for divalent (2:2) electrolytes.

Biological macromolecules are charged in an aqueous environment at physiological pH because of exposed weak acidic and basic functional groups which dissociate according to their p*K*.

Mica minerals are layered crystals (Bailey, 1984) with cleavage planes which are atomically flat over several hundred μm^2. Tetrahedral sheets of $(Si, Al)_2O_5$, are ionically linked by a central layer of $Al_2(OH)_2$ (Fig. 2). The net negative charge of the basal oxygens between these double layers is balanced by a layer of hexagonally coordinated cations (e.g., K^+ in muscovite, Na^+ in paragonite mica). This layer is disrupted after standard cleavage procedures (e.g., by means of scotch tape), exposing a basal plane covered by ions, K^+ in the case of muscovite mica (0.57 K^+ ions/nm^2). In air, this layer is completely neutralized by the negative aluminosilicate lattice charge (Gaines and Tabor, 1956). However, in water some of the K^+ ions dissociate from the surface, which results in a negative surface charge density of $\sigma_m \approx -0.0025$ C/m^2 or to 0.015 negative charges/nm^2 at neutral pH (Pashley, 1981). In solutions the extent of the dissociated and partially replaced K^+ ions depend on the electrolyte concentrations (Gaines and Tabor, 1956; Pashley, 1981).

To estimate the total force that drives the adsorption, we consider the sum of the electrostatic and the van der Waals forces. The total force per unit area between two flat, ultrasmooth surfaces according to the DLVO theory is

$$F_{DLVO}(z) = F_{el}(z) + F_{vdW}(z) = \frac{2\sigma_s\sigma_p}{\epsilon_e\epsilon_0} e^{-z/\lambda_D} - \frac{H_a}{6\pi z^3}, \qquad (4)$$

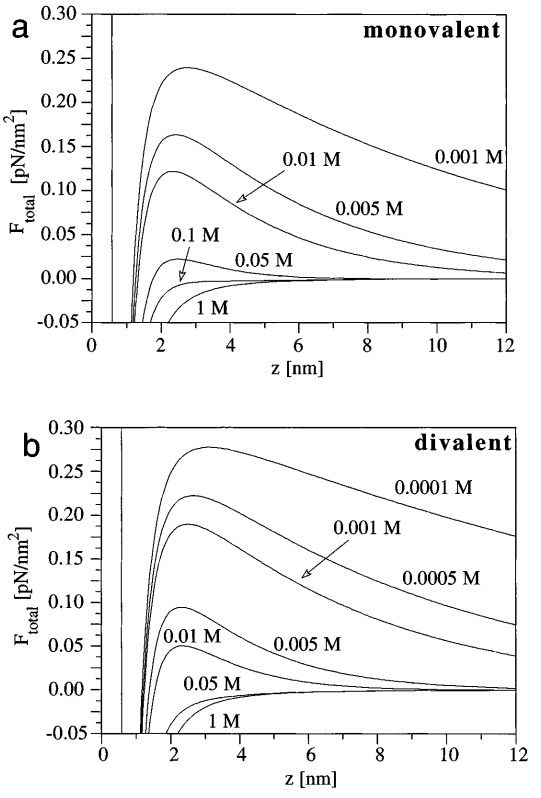

FIG. 3. Total force per unit area (1 nm^2) calculated [Eq. (4)] between purple membrane and the mica surface. F_{DLVO} was calculated according to the DLVO theory for different concentrations of the 1:1 electrolyte (a) and 1:2 electrolyte (b). While the attractive van der Waals force is mainly unaffected by the electrolyte [cf. Eq. (1)], the double-layer repulsion decreases with increasing salt concentration [cf. Eqs. (2) and (3)] and the membrane jumps directly into the van der Walls attraction with the mica. The surface charge densities were taken as -0.0025 C/m^2 for mica (Pashley, 1981) and -0.05 C/m^2 for purple membrane (Butt, 1992b). The Hamaker constant for hydrocarbons in water, 1×10^{-20} J (Butt *et al.*, 1995), was employed.

Equation (4) was evaluated numerically to determine the force between the surfaces of purple membrane and mica for monovalent (e.g., KCl, LiCl, NaCl) and divalent (1:2) (e.g., $CaCl_2$, $MgCl_2$, $NiCl_2$) electrolyte solutions. As illustrated in Fig. 3, the repulsive electrostatic force decreases with increasing electrolyte concentration until the attractive van der Waals force dominates. In this case purple membranes adsorb firmly to the mica surface, thereby minimizing the interaction energy (Israelachvili, 1991). These results are similar to the estimated and measured forces between a Si_3N_4 stylus (standard cantilever) and a mica surface in electrolyte solution. Here, the repulsive force also vanishes with increasing electrolyte concentration and the stylus is pulled down onto the mica surface (Butt, 1991, 1992a,b).

EXPERIMENTAL RESULTS AND DISCUSSION

Adsorption of Purple Membrane

In agreement with the above theoretical considerations the adsorption density of purple membrane (40 µg/ml) on freshly cleaved mica varied according

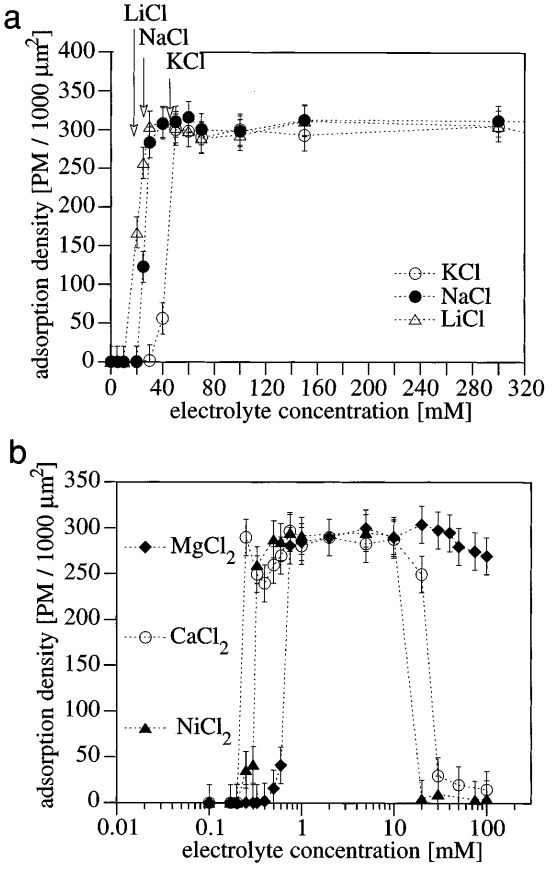

FIG. 4. Adsorption density of purple membrane to freshly cleaved mica in dependence of the electrolyte concentration. (a) Purple membrane (40 µg/ml) adsorbed in 1:1 electrolytes. With increasing electrolyte concentrations the maximum adsorption density was first achieved using LiCl, followed by NaCl and KCl. (b) Purple membrane adsorbed in 1:2 electrolytes. With increasing electrolyte concentrations the maximum adsorption was first achieved using $CaCl_2$, followed by $NiCl_2$ and $MgCl_2$. At salt concentrations above 10 m*M* ($CaCl_2$ and $NiCl_2$) and 50 m*M* ($MgCl_2$) the purple membranes aggregated and the ratio of single sheets adsorbed to mica decreased. Purple membrane was suspended in electrolyte (40 µg/ml protein concentration, milipore water) and deposited (50 µl) onto freshly cleaved mica discs (radii 6 mm) at room temperature. After an adsorption time of 5 min the samples were gently rinsed with the appropriate electrolyte and were ready to be monitored with the AFM.

to the type of electrolyte used and its concentration (Fig. 4). In the case of monovalent salts, the adsorption of the membrane sheets started at 15 ± 5 m*M* Li^+, 20 ± 5 m*M* Na^+, and 40 ± 5 m*M* K^+ (Fig. 4a). The maximum adsorption densities were achieved by further increasing the electrolyte concentrations by about 10 m*M*. Any further increase of the salt concentrations up to 300 m*M* did not result in a higher adsorption density. Using divalent (2:1) electrolyte, the adsorption of the membrane sheets was observed to start at electrolyte concentrations of 0.25 ± 0.1 m*M* Ca^{2+}, 0.3 ± 0.1 m*M* Ni^{2+}, and 0.6 ± 0.1 m*M* Mg^{2+} (Fig. 4b). Maximum adsorption densities were observed at concentrations more than 0.7 ± 0.1 m*M*. At electrolyte concentrations above 20 m*M* in case of Ca^{2+} and Ni^{2+}, or 50 m*M* in case of Mg^{2+}, the purple membranes aggregated. Therefore, the maximum adsorption density of purple membrane sheets could not be determined.

This demonstrates that the adsorption of purple membrane to mica can be manipulated by monovalent and by divalent electrolytes. Relatively low concentrations of divalent cations, about 50–100 times less than the respective concentration of monovalent salts, were necessary to attach purple membrane to mica. Divalent cations had a much more pronounced effect on the adsorption behavior of purple membrane because they produce a shorter Debye length than monovalent electrolytes [cf. Eq. (3)]. As also shown by other groups, divalent cations are thus especially well suited for attaching native biological macromolecules to a negatively charged support without further treatment of the sample (Butt *et al.*, 1990, 1991; Hoh *et al.*, 1993; Schabert *et al.*, 1994; Hansma and Laney, 1996). Divalent cations have been assumed to act as a bridge between two negatively charged surfaces (Butt *et al.*, 1991; Hansma and Laney, 1996; Shao *et al.*, 1996), but this model does not explain the attachment of negatively charged surfaces in the presence of monovalent cations. As demonstrated here DLVO forces govern the adsorption of biomolecules to mica.

The ion concentration required to facilitate adsorption increased in the sequence Li^+, Na^+, K^+, corresponding to their increasing ionic radii (cf. Table I). In contrast, the sequence with divalent ions was Ca^{2+}, Ni^{2+}, Mg^{2+}, i.e., the cation with the largest radius promoted binding of the sample at the lowest concentration of these three divalent ions (cf. Table I). This behavior was not predicted by the DLVO theory. It is based on the Poisson equation to describe the electrostatic attraction of the counterions to the surface and the Boltzmann distribution to account for the diffusion of the counterions. Fixed charges are assumed to be smeared out uniformly over the plane, and the electrolyte solution is modeled as a structureless medium with a uniform dielectric constant, while the ions in the solution are considered point charges (Israelachvili, 1991). Furthermore, the charge distribution of biological and supporting surfaces and structure effects of water

TABLE I

Crystallographic Radii of Ions (Israelachvili, 1991)

Monovalent ion	Radii (nm)	Divalent ion	Radii (nm)
Li^+	0.068	Mg^{2+}	0.065
Na^+	0.095	Ni^{2+}	0.072
K^+	0.133	Ca^{2+}	0.099

are not taken into account by the DLVO theory. Recent Monte Carlo simulations in which ions are considered as hard spheres show that potential profiles and electrolyte concentrations of surfaces are identical with calculations for point charges up to high electrolyte concentrations and surface charge densities (McLaughlin, 1989). This was experimentally demonstrated on phospholipid bilayers, where it was appropriate to ignore the finite size of ions if they were smaller than the Debye length, supporting the validity of the DLVO theory. However, the cation specific variations of the adsorption behavior presented here call for a refined theoretical analysis.

The pH of the buffer solution is an additional factor which can influence the adsorption of purple membrane (Fig. 5). At monovalent electrolyte (KCl) concentrations up to 30 m*M* no membranes adsorbed to mica between pH 2.6 and 10.4. This behavior changed at salt concentrations of 40 m*M*. While below pH 3 no membranes adsorbed onto mica, the adsorption slowly increased above pH 3.5 to reach its maximum at pH 5.0. At salt concentrations of more than 50 m*M* the variation of the pH did not influence the adsorption density of purple membrane. These results show the importance of the pH for the adsorption of purple membrane. At low pH a higher electrolyte concentration is required to adsorb the membranes than at higher pH values. This results from the change of surface charge densities of sample and support versus pH, depending on the p*I* of both surfaces. The p*I* of bacteriorhodopsin is centered at 5.2 and 5.6 (Ross *et al.*, 1989), while that of mica is at approximately pH 6.

Adsorption and Imaging of Biological Systems

According to these results, biomolecules and supramolecular assemblies can be immobilized on mica if the electrostatic repulsion is minimized. Depending on the properties of the biological sample this can be achieved by the variation of the electrolyte concentration and the pH of the buffer solution. As illustrated with the examples below, a variety of biological samples can be attached to freshly cleaved mica in this manner.

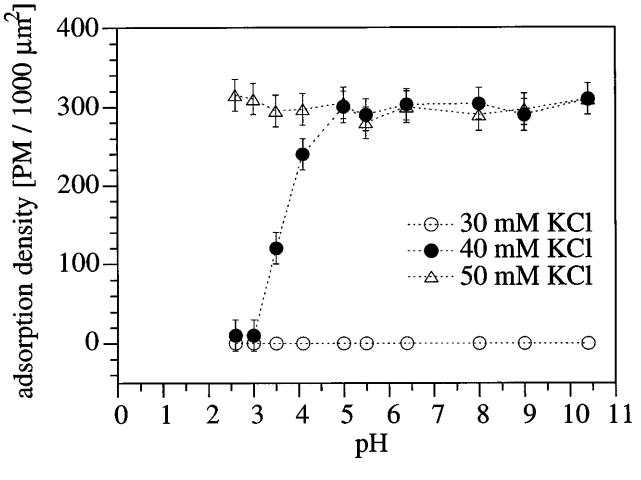

FIG. 5. Adsorption density of purple membrane to freshly cleaved mica in dependence of the pH of the buffer solution.

Amylin fibrillar assemblies. Amylin, a 37-amino-acid peptide (Cooper, 1994), is cosecreted with insulin from pancreatic β-cells in response to nutrient stimuli. It has structural relationships to two other messenger proteins, calcitonin and CGRP (Pittner *et al.*, 1994). Human amylin is cytotoxic at concentrations above 1–10 μ*M*. *In vitro* it aggregates to form fibrillar structures consisting of multiples of an underlying protofilament (Goldsbury *et al.*, 1996). The amount of protofilaments per fibre depend on the solution conditions.

Human amylin adsorbed to mica could be reproducibly imaged in buffer solution as tangled clumps (Fig. 6a). The fibrous structures were observed shortly after preparation of the amylin solutions. Assemblies formed independent of the pH, amylin concentration, and electrolyte (Goldsbury *et al.*, 1996). Fibrils were not firmly attached at monovalent electrolyte concentrations below 10 m*M*. Concentrations above 150 m*M* resulted in stable adsorption and allowed molecular resolution to be achieved (Fig. 6b). Small divalent electrolyte concentrations (1–2 m*M* Mg^{2+}, Ca^{2+}) were sufficient to compensate for the electrostatic repulsion. At pH 2.0 amylin adsorbed onto mica in the presence of 0.125 m*M* $ZnCl_2$ (Goldsbury *et al.*, 1997). The widths of the thinner fibers, consisting of two protofils, were four to five times larger than that determined by electron microscopy (≈8 nm; Goldsbury *et al.*, 1996). Some higher order coiled fibrils showed a width of more than 60 nm. Such broad filaments sometimes exhibited periodic protrusions separated by 60 ± 9 nm (gallery, Fig. 6a), confirming measurements by transmission electron microscopy (Goldsbury *et al.*, 1996).

Aquaporin-1. The human erythrocyte aquaporin-1 (AQP1) is a water channel-forming integral protein of 28 kDa from the red cell membrane (Agre *et al.*, 1993). As a major protein (2×10^5 copies per cell; Smith and Agre, 1991), it is responsible for a rapid swelling and shrinkage of the red blood cell. The osmotic water permeability of AQP1 allows $\approx 2 \times 10^9$ water molecules to pass a single channel per second (Walz *et al.*, 1994). Since AQP1 does not facilitate the passage of protons, ions, or urea, the water channel must possess a highly specific structure. A three-dimensional reconstruction of negatively stained AQP1 revealed a tetramer that contains a central depression about its fourfold axis (Walz *et al.*, 1994) on one side of the membrane and a

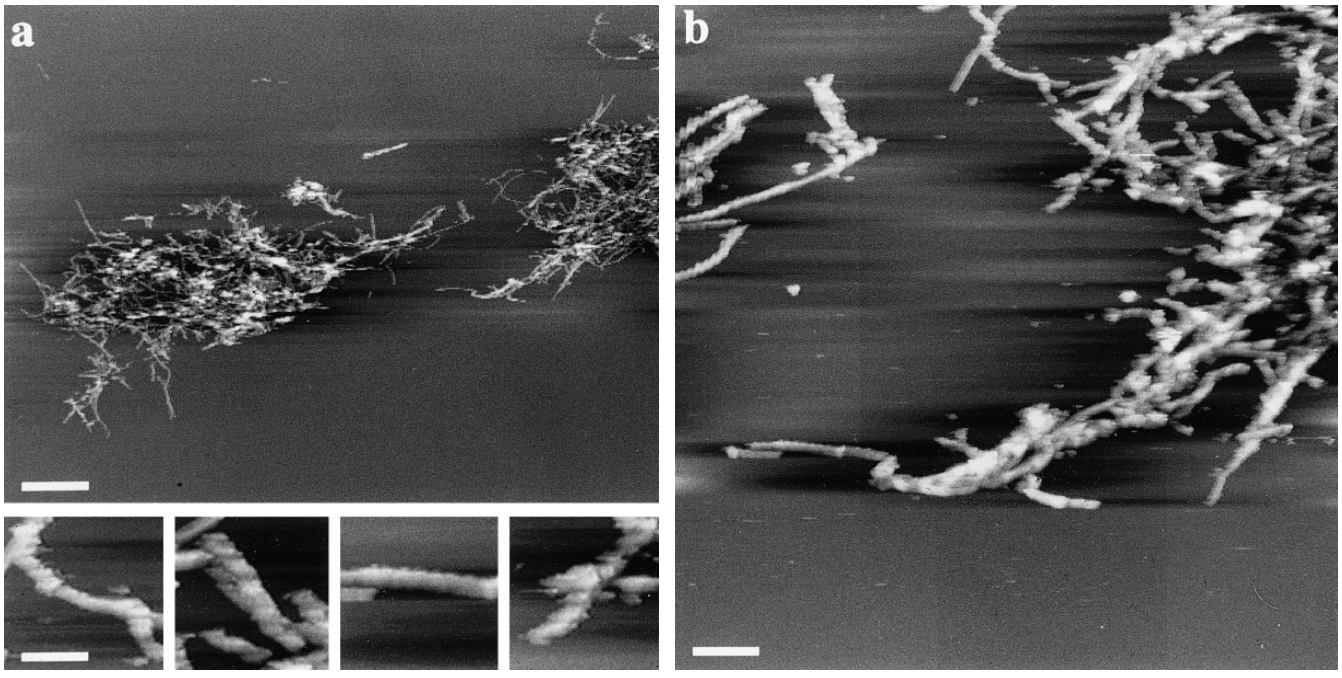

FIG. 6. Human amylin fibrillar assemblies attached onto freshly cleaved mica imaged in buffer solution. (a) The filaments formed tangled clumps. (b) At higher magnification the filamentous structures formed by the human amylin were more distinct. The insets shows fibres exhibiting longitudinal periodicity of 60 ± 9 nm. Full gray levels 40 and 20 nm in (b) and inset; scale bars 1.5 μm, 400 nm, and 200 nm for (a), (b), and inset, respectively. Conditions for adsorption and high resolution imaging: Adsorption buffer with monovalent salt concentrations above 150 m*M*, pH 7.4, 10 m*M* Hepes–NaOH; imaging buffer pH 7.4, 10 m*M* Tris–HCl, 50–100 m*M* KCl.

tetrameric on the other side. The isoelectric point of AQP1 calculated from the sequence is 6.95.

Firm attachment of AQP1 crystals onto freshly cleaved mica required more than 150 m*M* monovalent or 2–4 m*M* divalent electrolyte around neutral pH (6–8), indicating a higher surface charge density than purple membrane. Crystalline sheets immobilized in the presence of sodium chloride (150 to 500 m*M*) and/or $MgCl_2$ (2 to 10 m*M*) appeared to be corrugated, displaying wavelike structures. The lateral repeat of these waves was several tens to hundreds of nanometers. As presented previously for purple membrane, AQP1 sheets were found to attach flatly onto polylysine-coated mica (Müller *et al.*, 1995b). High-resolution images on these samples showed a lateral resolution between 1.7 and 2.0 nm. Further improvement of the adsorption conditions resulted in sheets that attached flatly to mica without polylysine which enabled us to achieve a lateral resolution better than 1 nm (Walz *et al.*, 1996). The direct attachment of the sheets onto mica was performed in presence of 300 m*M* KCl, 10 *M* Tris–HCl, pH 8.4 for 30 to 60 min. For high-resolution imaging the buffer was exchanged to 150 m*M* KCl, 10 m*M* Tris–HCl, pH 7.4.

Although reconstituted sheets of AQP1 formed stacks and larger aggregates, single sheets adsorbed flatly onto mica in buffer solution (Fig. 7a). After attachment onto mica the two-dimensional crystals remained stable in buffer solution for more than 5 days at room temperature. The height of such sheets was 5.8 ± 0.4 nm (n = 37). Large crystalline areas were imaged with molecular resolution (Fig. 7b). Point defects and lattice disorder were frequently observed. At high magnification the quadruple protrusions of the AQP1 tetramers, identified as cytoplasmic by proteolytic digestion (Walz *et al.*, 1996), were distinct (Fig. 7c). The rectangular unit cell ($a = b$ = 9.6 nm; white square, Fig. 7c) contains two tetramers of transmembrane AQP1 monomers that are incorporated in opposite orientations (Walz *et al.*, 1994). While the cytoplasmic protrusions can directly be seen, visualization of the small extracellular protrusions required image averaging (Walz *et al.*, 1996).

HPI layer. The hexagonally packed intermediate layer (HPI), a typical bacterial surface layer, represents the major cell envelope protein of the radiotolerant bacterium *Deinococcus radiodurans* (Baumeister *et al.*, 1982). The HPI layer has been characterized biochemically (Baumeister *et al.*, 1982), by electron microscopy (Baumeister *et al.*, 1986), and by atomic force microscopy (Karrasch *et al.*, 1994; Müller *et al.*, 1996a). Assembled from one protein (M_r 107 028; Peters *et al.*, 1987) forming hexamers of M_r 655 000

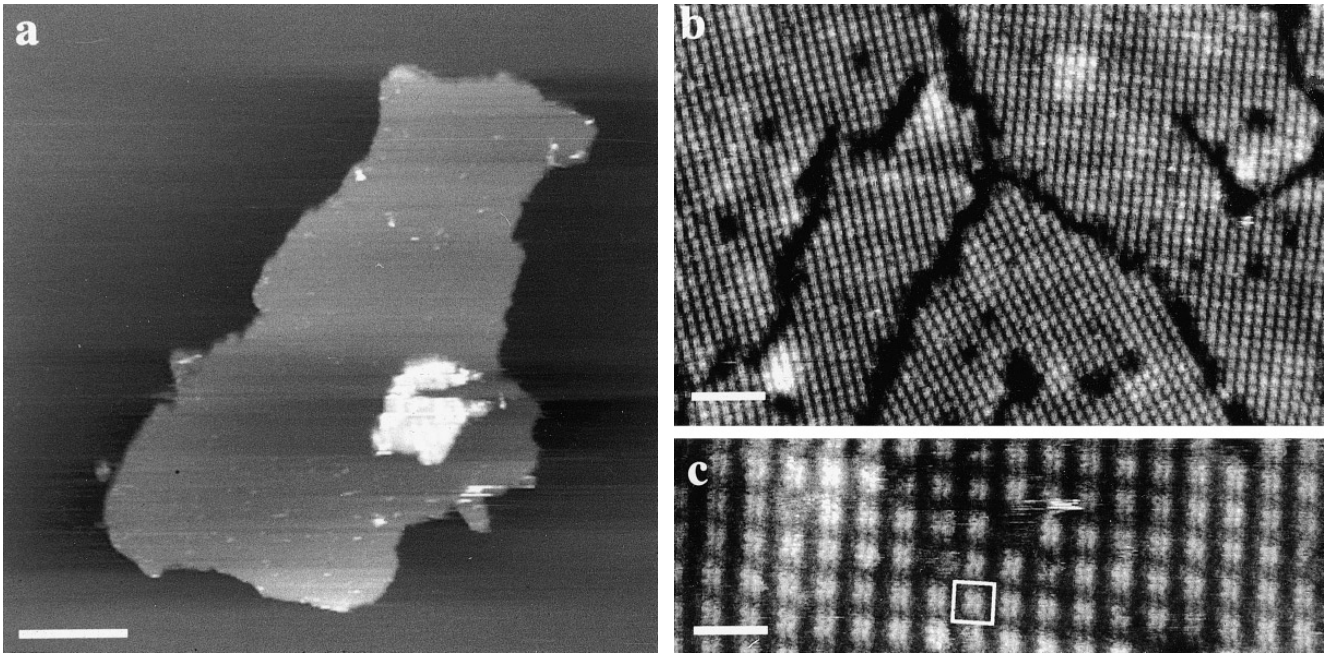

FIG. 7. Reconstituted crystal monitored in buffer solution. Two-dimensional AQP1 crystals adsorbed to freshly cleaved mica in pH 8, 10 m*M* Tris–HCl, 300 m*M* KCl. Membranes that were not firmly attached to the mica were removed by gently rinsing the sample with the imaging buffer solution (pH 8.2, 10 m*M* Tris–HCl, 150 m*M* KCl). (a) The surveys showed large, flatly attached sheets. (b) At higher magnification the square lattice was distinct. Due to its $p422_1$ symmetry both surfaces of the crystal were similar and the high-resolution topography (c) shows up the cytoplasmic protrusions of every second AQP1 tetramer. Full gray levels 50, 3, and 2 nm; scale bars 1 μm, 80 nm, and 20 nm for (a), (b), and (c), respectively.

(Engel *et al.*, 1982), the HPI layer forms a hexagonal lattice with a unit cell size of 18 nm. According to the three-dimensional model from electron microscopy (Baumeister *et al.*, 1986) one hexagonal unit is composed of a massive core which encloses a pore and from which six thin spokes emanate to connect adjacent units.

Due to their unusual stability (Baumeister *et al.*, 1982), HPI layers can be adsorbed under various conditions to different supports. For their proper attachment onto mica a minimum of 100 m*M* monovalent electrolyte was required at pH 7. Monovalent electrolyte concentrations larger than 100 m*M*, or the addition of divalent electrolytes (2–20 m*M;* $MgCl_2$ or $CaCl_2$) did not significantly alter the adsorption behavior of the HPI layers. Adsorption buffer containing exclusively divalent electrolytes, however, caused the HPI layers to form stacks and/or prevented them from attaching flatly to mica.

HPI layers always adsorbed onto mica with the hydrophilic outer surface (Baumeister *et al.*, 1986) facing the hydrophilic support (Fig. 8; Müller *et al.*, 1996a). Thus, the hydrophobic inner surface of a single HPI layer was exclusively accessible to the AFM tip. In contrast, the inner HPI surface exclusively attached to the support when chemically activated hydrophobic glass surfaces were used (Karrasch *et al.*, 1993), thereby allowing structural analysis of the extracellular surface. Adsorbed on to mica, the height of a single layer was 7.0 ± 0.5 nm, but interestingly the measured height of double-layer stacks was 17.4 ± 0.8 nm (Müller *et al.*, 1996a). Stacking of the layers involves contacts between either the hydrophobic or the hydrophilic surfaces. Even-numbered stacks thus exposed the outer surfaces. When two adjacent layers adsorbed to mica overlapped at their edges, the inner and the outer surface of the HPI layers were directly in contact, and the measured height was 14.7 ± 0.5 nm, as expected from the thickness of the single layer. The increased height measured for stacks cannot be explained other than by specific interactions between the protein surfaces (Müller *et al.*, 1996a).

At higher magnification the hexagonal arrangement of the protomers was distinct (Fig. 8b). Monitored at minimal forces (<200 pN) the layers were stable over hours while scanned with the stylus. The inner surface show two conformations, a "closed" and an "open" pore (Fig. 8c). These conformations were reversible and changed with time (Müller *et al.*, 1996a). At high resolution the topography of the outer surface clearly exhibits the V-shaped protrusions of the protomers at top of the cores, as well as the emanating arms (Fig. 8d).

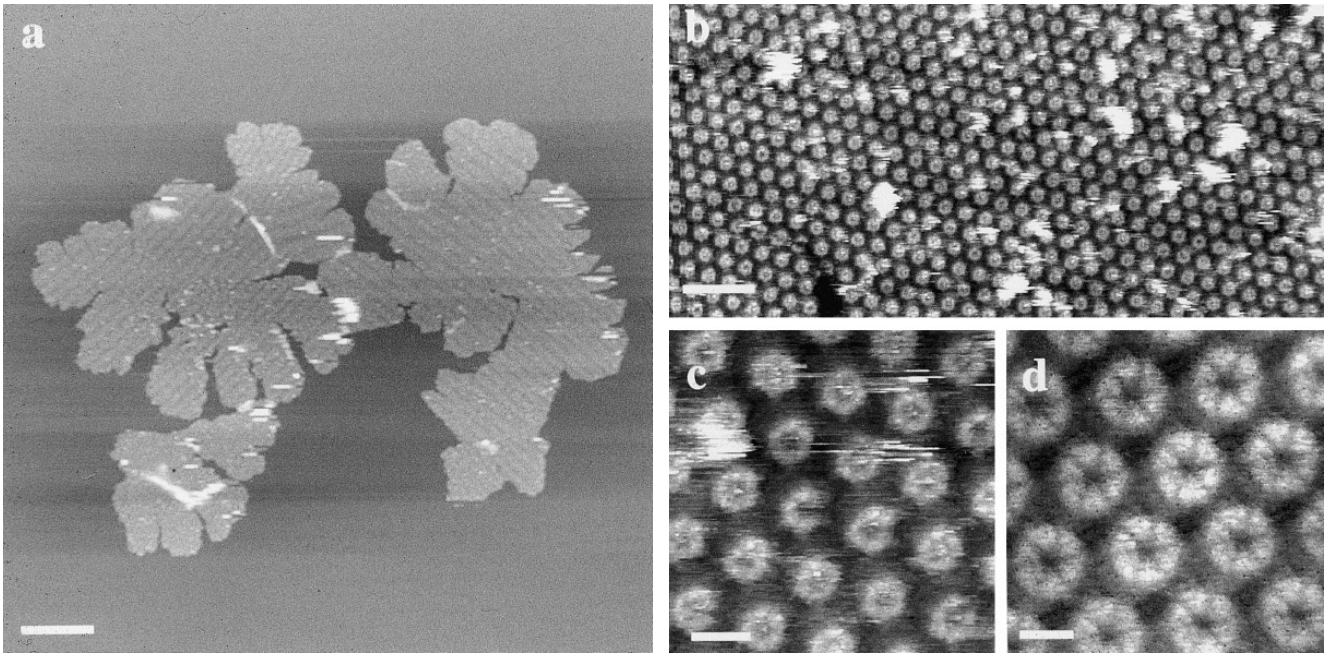

FIG. 8. HPI layers flattly attached to mica monitored in buffer solution with the AFM. (a) The survey shows the topography of a single HPI layer. (b) At higher magnification the hexagonal arrangement of the cores is distinct. High-resolution images (c) and (d) of the inner and outer surface of the HPI layer show the subunits of the cores and their arms emanating to the adjacent units. Two conformations of the pores of the inner surface (c) were distinct. The open pore can reversibly switch to a closed conformation (Müller *et al.*, 1996a). Full gray levels 30, 4, 5, and 3 nm, while scale bars represent 500, 50, 15, and 10 nm in (a), (b), (c), and (d), respectively. Optimized conditions for adsorption and high-resolution imaging: Adsorption buffer pH 7.4, 10 m*M* Tris–HCl, 300 m*M* KCl; imaging buffer pH 8.2, 10 m*M* Tris–HCl, 150 m*M* KCl.

Liposomes. Thermoacidophilic archaeon *Sufolobus acidocaldarius* grows in hot acid springs at pH values between 2 and 3 and temperatures of 85°C. Tetraether lipids span the whole cytoplasmic membrane and protect the cell against this harsh environment (Elferink *et al.*, 1994). Additional rigidity of the cell envelope is provided by a S-layer covering the outside of the cytoplasmic membrane to which it is anchored by glycoproteins. The tetraether lipid layer contains at least 11 different lipid species (Elferink *et al.*, 1992). Approximately 70% of these are phosphoglycolipids with galactose or glucose facing the outside of the membrane and a negatively charged phosphate inositol facing the cytoplasm. However, liposomes have lost this asymmetry in headgroup orientation because they carry a negative surface charge.

The best results were achieved after immobilizing the liposomes on freshly cleaved mica in 80 m*M* KCl, 20 m*M* $MgCl_2$, 10 m*M* Tris–HCl, at pH 7.2. Intact liposomes were then distributed uniformly on the surface and could be reproducibly imaged at forces below 100 pN, but lead to streaky images as result of their flexibility (Fig. 9a). At higher forces (>250 nN) some liposomes were swept away by the interaction with the stylus, while others popped open and adsorbed as lipid layers (Fig. 9b). The lipid membranes showed a size distribution which correlates well with the distribution of the liposome diameters measured by photon correlation spectroscopy (Elferink *et al.*, 1994). The average height of the bilayers was 5.6 ± 0.3 nm (n = 22). Due to their unusual stability the liposomes could be attached to mica at values between pH 2 and 9 using monovalent electrolytes up to 1 *M*. The minimum monovalent electrolyte concentration required for adsorption was about 300 m*M*. However, divalent ions mediated a stronger attachment of the liposomes to the mica than monovalent ions.

Phosphatidylethanolamine. Phosphatidylethanolamine (PE) represent one dominant phospholipid species of bacterial membranes and many other biological membranes. The headgroup of PE contains one positive (aminogroup) and one negative (phosphategroup) charge. Therefore, the net charge is zero, and the head group has a dipolemoment. DPPE has two C_{16} fatty acid chains, its p*I* is 11.25 (Cevc and Marsh, 1985), and the transition temperature lies at 64°C. DPPE bilayers deposited on mica by the vesicle fusion method (Vikholm *et al.*, 1995) are shown in Fig. 10. The covering density was 70%, depending on the temperature, the amount of DPPE, and the buffer solution. At 300 m*M* KCl, 20 m*M*

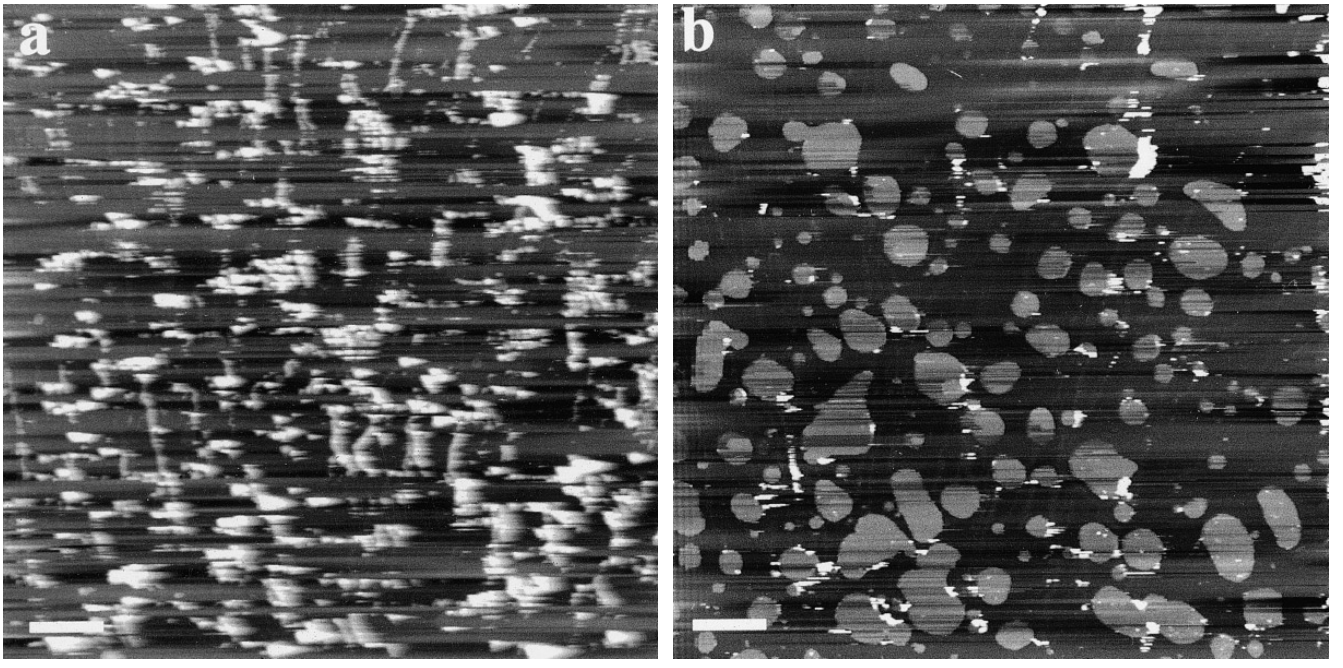

FIG. 9. Liposomes adsorbed onto mica in buffer solution. (a) Imaged at forces below 100 pN the intact liposomes protruded up to 100 nm from the mica, but were not sufficiently stable to produce clear images. (b) When the same area was imaged at forces of about 200 pN some of the liposomes were swept away by the stylus, while others "spread-flattened" onto the mica. The bilayers showed a height of 5.6 ± 0.3 nm (n = 22). Full gray levels are 100 and 50 nm, and scale bars represent 2 μm in (a) and (b), respectively. Optimized conditions for adsorption and imaging: Adsorption buffer pH 7.4, 10 m*M* Tris–HCl, 80 m*M* KCl, 20 m*M* $MgCl_2$; imaging buffer pH 7.2, 10 m*M* Tris–HCl, 150 m*M* KCl.

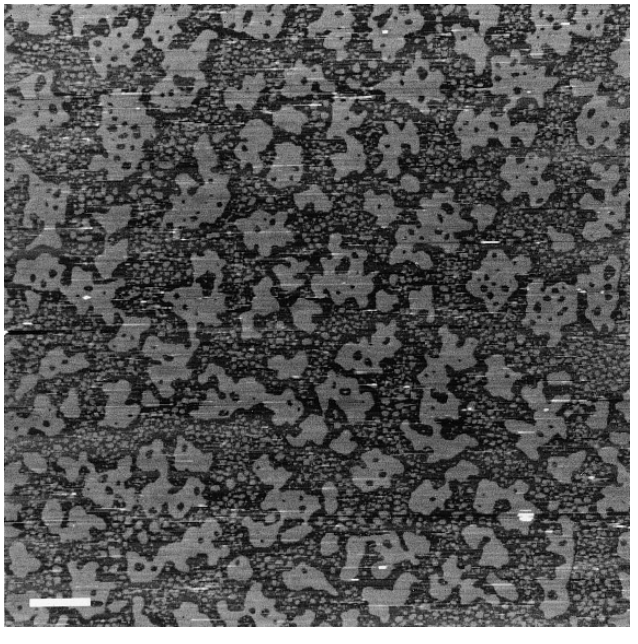

FIG. 10. Phosphatidylethanolamine attached from the buffer solution onto mica. The bilayers showed a height of 5.2 ± 0.4 nm (n = 84). Scale bar 1 μm, full gray level 15 nm. Optimized conditions for adsorption and imaging: Adsorption buffer pH 7.4, 10 m*M* Tris–HCl, 10–20 m*M* KCl; imaging buffer pH from 3 to 10, adjusted in 10 m*M* citric acid, 10 m*M* Hepes, 10 m*M* Tris, and substituted with 40 to 300 m*M* KCl or NaCl.

Tris–HCl, pH 8.4, the height of the bilayer was 5.2 ± 0.4 nm (n = 84).

Because of their small positive charge at pH < 11.25 (Cevc and Marsh, 1985) the DPPE layers adsorbed at very low salt concentrations (5–50 m*M* monovalent electrolyte) to freshly cleaved mica. However, the best results were achieved by adsorbing DPPE onto mica in the presence of more than 10–20 m*M* divalent electrolyte around neutral pH (6–8). Because the DPPE bilayers showed a high stability, the electrolyte and the buffer conditions could then be changed to monovalent electrolyte concentrations from 1 m*M* to 1 *M* and pH values ranging from 2 to 11 without changing the quality of the bilayers (Fig. 10).

Photosystem II. Photosystem II is a major protein of the thylakoid membrane of chloroplasts and catalyses the water-splitting reaction associated with photosynthesis. The complex can be divided into the core fraction which comprises approximately 13 polypeptides (Tsiotis *et al.*, 1996) and the antenna fraction containing the light harvesting chlorophyll a/b binding proteins. The solubilized oxygen evolving photosystem II core complex isolated from spinach leaves shows an intrinsic quasi twofold symmetry (Tsiotis *et al.*, 1996; Hasler *et al.*, 1997).

Photosystem II complexes attached to the mica surface just firmly enough to be scanned in buffer solution at neutral pH and a monovalent salt concen-

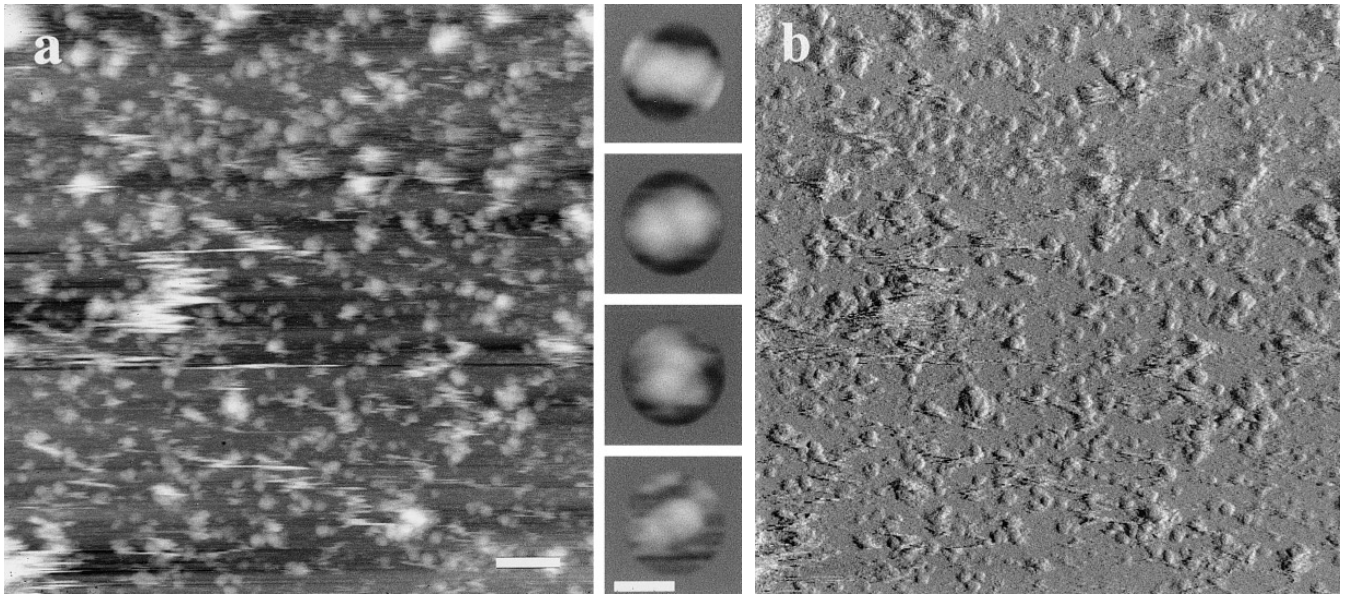

FIG. 11. Photosystem II complexes immobilized onto mica. (a) Height mode and (b) error mode show single molecules and aggregates. Selected particles of (a) are shown in the gallery. Full gray levels 20 nm in a and b and 5 nm in the gallery. Scale bars, 75 nm in (a) and 20 nm in the gallery. Optimized conditions for adsorption and high-resolution imaging: Adsorption buffer pH 7.2, 10 m*M* Hepes–NaOH, 10–50 m*M* NaCl or KCl; imaging buffer pH 7.2, 10 m*M* Hepes–NaOH, 5–10 m*M* NaCl or KCl.

tration above 5 m*M* (Fig. 11). The complexes could be imaged reproducibly at low resolution, but were swept away by the scanning stylus at vertical forces >100 pN. An increase of the electrolyte concentration did not improve the immobilization, indicating that in this case the adsorption energy was mainly determined by van der Waals forces. Because of this instability, higher resolution images of single particles could not be acquired. The particles exhibited a significant inhomogeneity in size and shape (insets, Fig. 11), even more pronounced than that observed by electron microscopy after negative staining (Hasler *et al.,* 1997). Larger particles were probably aggregated photosystem II complexes, whereas the smallest particles could not be identified. However, many particles had an elongated bilobed shape and dimensions that were consistent with data from electron microscopy. In spite of tip effects these particles could be measured reliably and had a length of 20 ± 5 nm and a width of 10 ± 5 nm, while their height was determined to 4 ± 1 nm. The lateral dimensions compare favorably with the data from electron microscopy (l = 14 nm, w = 10 nm; Hasler *et al.,* 1997), while the hight is smaller than expected for an integral membrane protein complex with significant protrusions.

Porin OmpF. Porin OmpF is a trimeric channel forming protein in the outer membrane of the *E. coli* cell. It facilitates the diffusion of hydrophilic molecules ($M_r < 600$) in both directions across the membrane, is weakly cation selective, and exhibits voltage-gated channel activity (Lakey, 1987). Moreover, the channel conductivity is pH dependent (Todt *et al.,* 1992). The structure of porin OmpF has been solved by X-ray crystallography (Cowan *et al.,* 1992). Each monomer comprises a barrel made of 16 antiparallel β-strands that form a channel through which nutrients can diffuse. The strands are connected by short loops on the periplasmic side, but loops of variable length on the extracellular side. The longest loop folds back into the channel, thereby restricting the ion flow. The other loops form a domain that protrudes by 1.2 nm from the bilayer (Schabert *et al.,* 1995).

Rectangular 2D crystals reconstituted from porin OmpF trimers and phospholipids (Hoenger *et al.,* 1993) attached flatly onto the mica surface in 300 m*M* KCl, 20 m*M* Tris–HCl, pH 8.2 (Fig. 12a). Similar results were achieved using buffer solutions containing 2 to 20 m*M* divalent and more than 100 m*M* monovalent electrolytes (pH from 6 to 8). These conditions agree with those from Schabert *et al.* (Schabert and Engel, 1994; Schabert *et al.,* 1994, 1995), who immobilized porin sheets in the presence of small amounts of divalent ions (2 to 2.5 m*M*, $MgCl_2$) and monovalent ions between 100 and 150 m*M*. We found reconstituted porin crystals to remain attached to mica firmly during several days over a pH range from 2 to 11 in the presence of divalent and/or monovalent ions.

We observed that single porin OmpF sheets preferentially adsorbed with their periplasmic surface

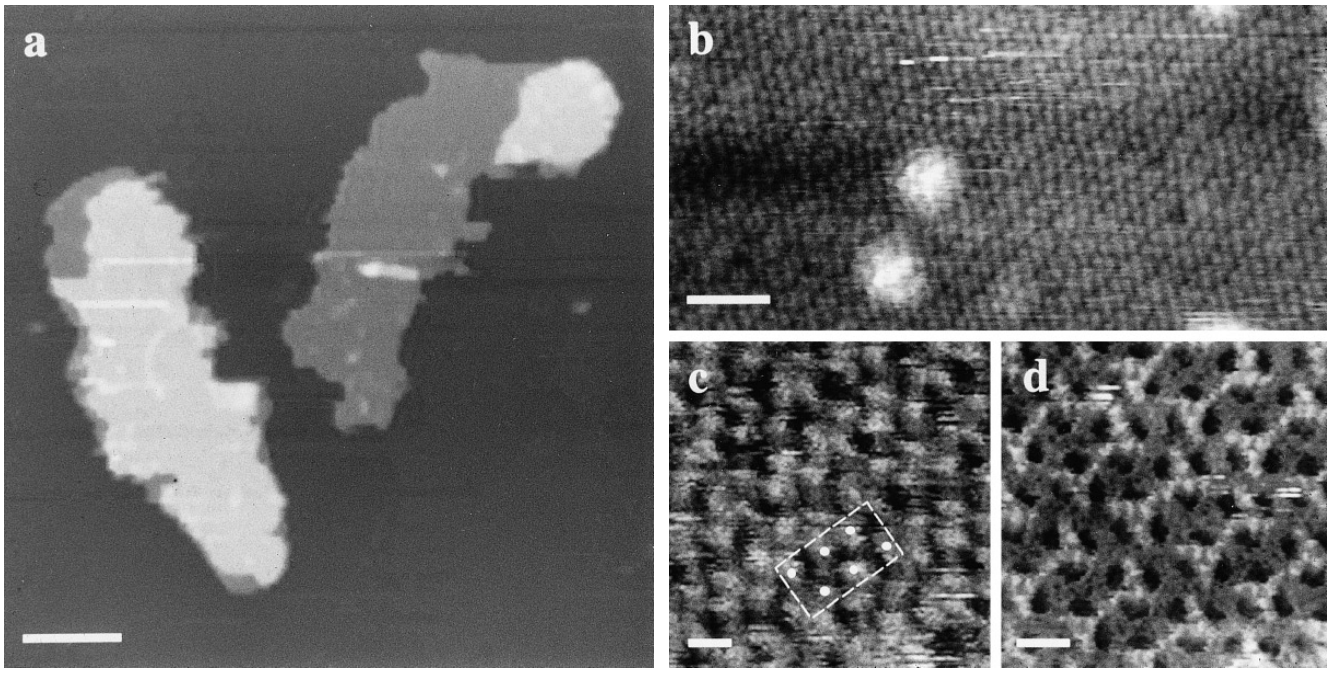

FIG. 12. Reconstituted porin OmpF sheets. (a) Sheets attached flatly onto mica using monovalent electrolytes. (b) The extracellular surface could be imaged with molecular resolution; the rectangular arrangement of porin trimers was distinct. The high-resolution images showed submolecular details of the extracellular (c) and the perisplasmic (d) surfaces of the trimers. Full gray levels are 50, 3, 2.5, and 2 nm, where scale bars represent 500, 50, 5, and 5 nm for (a), (b), (c), and (d), respectively. The best conditions for adsorption and high-resolution imaging were found to be at pH 7.2, 20 m*M* Tris–HCl, 300 m*M* KCl.

facing the mica. The height measured in 300 m*M* KCl, 20 m*M* Tris–HCl, pH 8.2, was 11.2 ± 0.4 nm (n = 42) for a double layer and 5.6 ± 0.4 nm (n = 34) for a single layer, in excellent agreement with results published by Schabert *et al.* (1995). On the relatively smooth periplasmic surface, which protrudes less than 0.5 nm from the lipid bilayer, a point resolution of better than 1 nm was achieved (Fig. 12d). Structural details of the porin trimers comprising three channels that were separated by walls 1.2 nm thick were distinct in unprocessed images. Between the three protrusions close to the threefold axis small depressions can be seen that are separated by less than 1 nm. The extracellular surface of the porin trimer (Fig. 12c) shows three domains which protruded by 1.2 nm from the lipid bilayer and were separated by 4.3 nm. The trimers were less distinct than on the periplasmic side as result of the packing arrangement. Although there is a characteristic small indentation in most of the protruding domains, the resolution achieved is smaller than on the periplasmic surface, because the extracellular loops are long and flexible.

Purple membrane. Purple membrane is a constituent of the inner membrane of *H. salinarium* and consists of 75% bacteriorhodopsin (M_r 26,500), a light-driven proton pump, and of 25% lipids (Kates *et al.*, 1982). Bacteriorhodopsin molecules are naturally arranged in a highly ordered 2D trigonal lattice ($a = b$ = 6.2 nm) and consist of seven transmembrane α-helices (Henderson *et al.*, 1990) surrounding the photoreactive retinal (Jubb *et al.*, 1984). Some of the α-helices can undergo conformational changes during the photocycle (Dencher *et al.*, 1989; Subramaniam *et al.*, 1993). Although the structure of bacteriorhodopsin is known to a resolution of 3.5 Å (Grigorieff *et al.*, 1996) some loops connecting transmembrane α-helices are flexible and cannot be imaged at atomic resolution. Here, surface topographs recorded at subnanometer resolution with the AFM (Müller *et al.*, 1995b) can provide additional information. Furthermore, force-induced reversible conformational changes of single loops have been monitored with the AFM (Müller *et al.*, 1995a). These results suggest that this technique may permit to directly assign function related conformational changes of these loops indicated by other methods (Steinhoff *et al.*, 1994, 1995).

Purple membrane naturally exists in 2 *M* NaCl solutions and is stable over a pH range from 2 to 11. Therefore, it can be investigated with the AFM under extreme conditions without denaturation. The membrane shown in Fig. 13a was adsorbed to mica in 10 m*M* Tris–HCl, pH 8, 150 m*M* KCl, but as illustrated in Figs. 4 and 5, purple membranes can be adsorbed and imaged using a wide range of

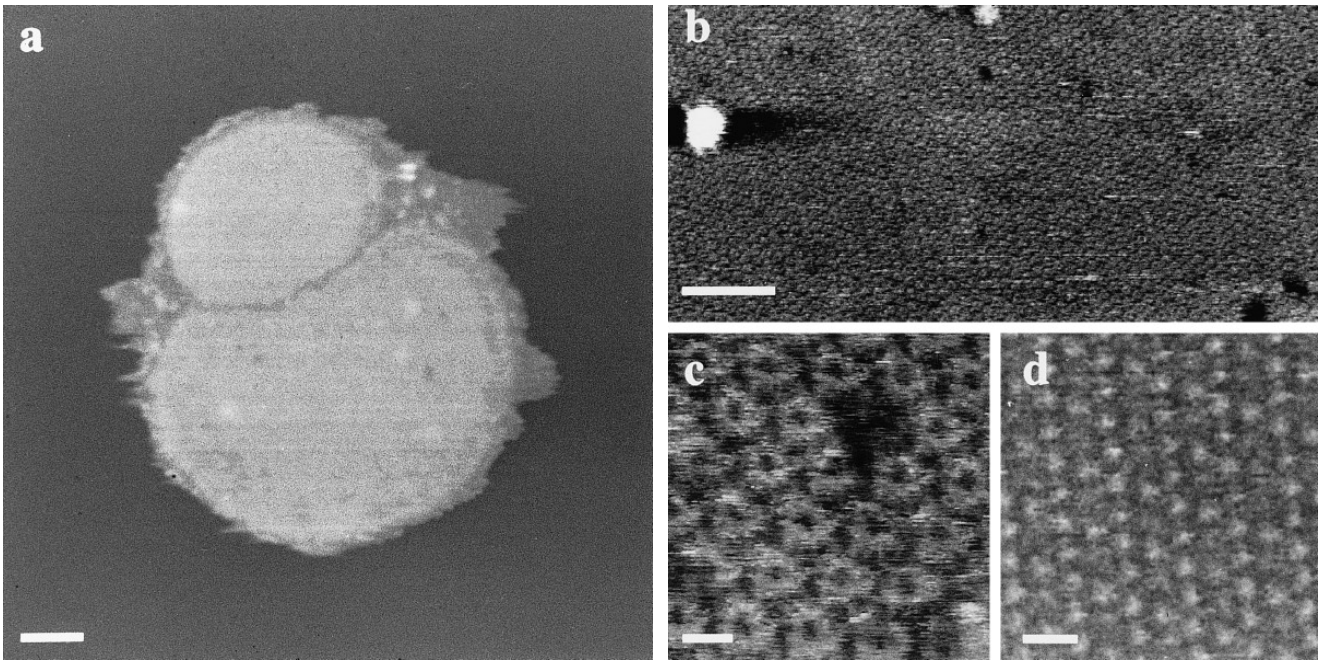

FIG. 13. Native purple membrane depicted with the AFM. The survey (a) shows two membrane sheets flatly attached to the freshly cleaved surface of mica. At higher magnification (b) the donut shaped structure of bacteriorhodopsin trimers is distinct. The high-resolution images (c) and (d) of the cytoplasmic and the extracellular surface purple membrane show the substructure of the bacteriorhodopsin molecules. Full gray levels are 50, 2, 2, and 1 nm, while scale bars represent 150, 50, 5, and 5 nm in (a), (b), (c), and (d), respectively. The best conditions for adsorption and high-resolution imaging: The adsorption buffer may vary from 4 to 10 at KCl or NaCl concentrations between 50 and 500 m*M;* the ideal imaging buffer is pH 8.2–9.2, 10 m*M* Tris–HCl, 150 m*M* KCl. Nevertheless, even under extreme electrolyte concentrations (e.g., 2 *M* NaCl) it was possible to achieve submolecular resolution.

electrolytes and pHs. For high resolution imaging the membranes must be attached firmly and flatly to the substrate (Müller *et al.,* 1995a, 1996b; Figs. 13b–13d). The height of the purple membrane was measured to 5.6 ± 0.2 nm under the conditions specified above, but depending on the buffer solution and the supporting surface, the measured heights can vary from 5.2 to about 11 nm (Butt *et al.*, 1990, 1991, 1992b; Müller *et al.,* 1995b). This height anomaly results from electrostatic repulsion between sample and stylus, i.e., the same kind of force that governs adsorption (Müller and Engel, 1997c). Figure 13b displays the topography of the cytoplasmic purple membrane surface with the highly ordered arrangement of bacteriorhodopsin trimers. Although bacteriorhodopsin is a very stable protein (Haltia and Freire, 1995), the applied force often had to be corrected manually during scanning to achieve stable images without deformation of the molecules (Weisenhorn *et al.*, 1993). At high magnification and a force applied to the tip of 300 pN, the cytoplasmic surface of one trimer appeared as doughnut-shaped protrusion (Fig. 13c). Sometimes an entire trimer was missing, as documented by Fig. 13. In addition, fine arms connecting trimers are distinct in Fig. 13c, but they are disordered and their signal is lost upon averaging (Müller *et al.,* 1995a). Imaged at 100 pN, the trimers reversibly transform into a more pronounced trimeric structure (data not shown). This phenomena was identified as bending of the loop E–F of the cytoplasmic surface (Müller *et al.,* 1995a). A smooth topography was characteristic for the extracellular surface (Fig. 13d), with an unit cell exhibiting a major and a minor trimeric protrusion. The height of the corrugations was about 0.22 nm, much less than the 0.6 nm measured at the cytoplasmic surface.

ø29 connectors. Head and tail of bacteriophages are joined by a connector that also plays a role in DNA packaging and translocation (Valpuesta and Carrascosa, 1994). Several head-tail connectors have been studied by electron microscopy and found to possess a narrow cylindrical end that interacts with the tail, and a wide cylindrical end that interfaces with the head. By 3D reconstruction a central channel has been observed (Carazo *et al.*, 1985) that is probably required for translocating the DNA (Carrascosa *et al.*, 1990). Connectors exhibit 12-fold (Driedonks *et al.*, 1981; Carrascosa *et al.,* 1982; Kochan *et al.*, 1984; Carazo *et al.*, 1986; Valpuesta *et al.,* 1994; Kocsis *et al.*, 1995; Cerritelli and Studier, 1996) as well as 13-fold (Dube *et al.*, 1993; Tsuprun *et al.*, 1994) rotational symmetry. This interesting polymorphism fostered different models for the DNA

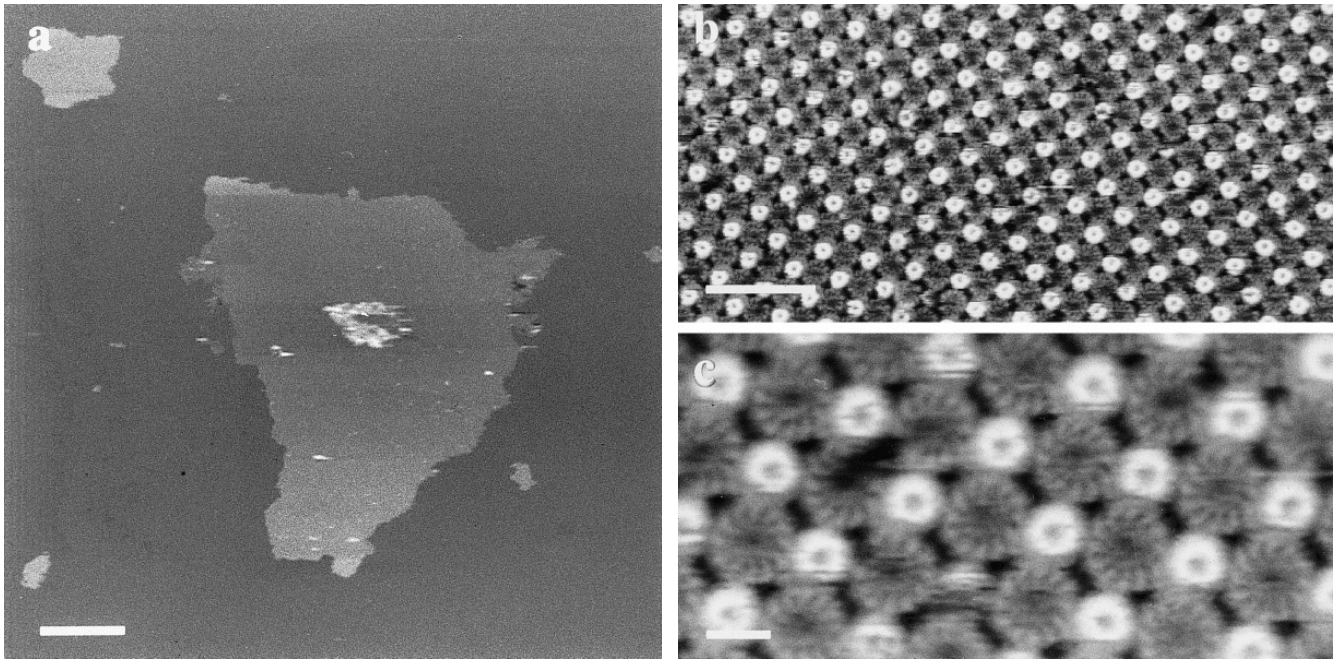

FIG. 14. Two-dimensional crystal of Ø29 bacteriophage connectors. The overview (a) shows the crystal flattly attached to the mica surface. Molecular resolution of the crystal surface (b) shows the tetragonal arrangement of the connectors. The high-resolution image of the connectors (c) reveals the submolecular details of the wide connector end such as the 12-fold rotational symmetry and the distinct handedness. The thinner end and the wide end of connectors represent one unit cell with a $p42_12$ symmetry. Full gray levels are 50, 5, and 3 nm, while scale bars represent 2 µm, 50 nm, and 10 nm in (a), (b), and (c), respectively. Best adsorption conditions: pH 7.2, 20 m*M* Hepes–NaOH, 1 *M* KCl. imaging conditions: pH 8.4, 20 m*M* Tris–HCl, 0.5 *M* KCl.

packaging mechanism. Necks of bacteriophage ø29 that consist of the connector protein and an additional subunit exhibit a 12-folded rotational symmetry and represent the native DNA packing protein. The ø29 connectors can be crystallized into highly ordered 2D crystals that have been studied by cryo-electron microscopy to a resolution of 0.9 nm (Valpuesta *et al.*, 1994).

Figure 14a shows crystalline sheets of ø29 connectors firmly adsorbed to mica. The best adsorption solution contained approximately 1 *M* monovalent salt concentrations at pH 8. If the salt concentration was to low (<500 m*M* monovalent salt), the 2D sheets showed cracks and lacked proper contact to the mica, thus preventing high-resolution imaging. This effect is necessarily the result of high surface charges at the connector ends, but is related to the stability of the crystals that require high salt concentrations (Valupesta *et al.*, 1994). Sheets adsorbed in 20 m*M* Hepes–HCL, pH 7, 1 m*M* KCl, showed diameters up to several tens of micrometers and remained stably attached to mica over several days in buffer solution (20 m*M* Tris–HCl, pH 8.4, 0.5 *M* KCl). The height of single sheets was 8.3 ± 0.6 nm (n = 49), whereas double layers exhibited a height of 16.8 ± 0.9 nm (n = 20). At higher magnification the rectangular connector lattice became visible (Fig. 14b). However, connector crystals were rather fragile and disintegrated within a few scans when the force applied to the tip exceeded 200 pN. As shown in Fig. 14c, one unit cell ($a = b$ = 16.5 nm) consisted of a connector pointing its narrow end up and a connector exposing its wide domain to the tip. To achieve high-resolution images of the wide ends, the narrow ends of the connectors facing the tip had to be pushed out of the way toward the crystal surfaces, thereby facilitating the contact between tip and wide connector ends. Large fields could be imaged in this manner to visualize the 12 subunits as well as the vorticity of the wide connector ends (Müller *et al.*, 1997a). The narrow ends were pushed away at a force of 100 pN, but this force induced structural change was found to be fully reversible.

CONCLUSION

We discussed the forces involved in adsorbing proteins and lipids to freshly cleaved mica. This frequently used method of sample preparation is particularly suitable for AFM in buffer solution (Butt *et al.*, 1991; Hoh *et al.*, 1993; Schabert *et al.*, 1994; Müller *et al.*, 1995a, 1996b, 1997a,c; Fritz *et al.*, 1995a,b; Vikholm *et al.*, 1995; Walz *et al.*, 1996; Hansma and Laney, 1996). Muscovite mica is one member of the large layered crystals family that includes micas (Bailey, 1984), highly oriented py-

rolitic graphite (HOPG), and transition metal dichalcogenides (Wilson and Yoffe, 1969). These solids all are chemically relatively inert and atomically flat over hundreds of μm^2. They display an enormous variety of electrical and physical properties and are therefore ideal supports for scanning probe microscopy.

Although the method allows single particles and filamentous samples to be adsorbed to mica, high resolution (<1 nm) could only be achieved with 2D protein crystals. This is most likely related to the stable immobilization resulting from the large surface area interacting with the support. High resolution has been demonstrated with GroES adsorbed to mica, a small oligomer assembled from seven 10-kDa proteins. The particles were rather densely packed, and high-resolution imaging was only possible after glutaraldehyde treatment (Mou *et al.*, 1996). Actin filaments and microtubules have been imaged after adsorption to mica, but in this case tapping mode AFM was used to prevent displacement of the sample (Fritz *et al.*, 1995a,b). Tapping mode imaging has also been key to imaging DNA physisorbed to mica (Hansma *et al.*, 1992 & 1995). These examples document that the preparation technique described here is of general use for all biological scanning probe microscopes. While single particles and filaments may be immobilized more stably by chemical crosslinking (Karrasch *et al.*, 1993; Wagner *et al.*, 1995, 1996), physisorption is more likely to preserve the biomolecule in a functional state.

Adsorption and subsequent high-resolution imaging of biological samples may require different conditions. For example, the optimum adsorption solution for the ø29 connector crystals contained 1 *M* KCl, but the best images were obtained in 0.5 *M* KCl. AQP1 adsorbed best in 300 m*M* KCl, but the best images were recorded in 150 m*M* KCl. These results emphasize that adsorption and imaging condition are not necessarily identical. Furthermore, the symmetry of the tip–sample and the sample–support interactions should be considered. This results from the similar surface properties of mica and the Si_3N_4 tip. This may well explain the difficulties in achieving subnanometer resolution of native single proteins physisorbed onto mica. In this case the interaction forces between protein and tip is of similar magnitude as those between protein and support. Proteins can thus easily be displaced by the scanning tip preventing the acquisition of high-resolution images. The interactions are different if the proteins are incorporated into a lipid bilayer. It follows that higher resolution of single particles may be achieved if they were adsorbed to a support showing different surface properties than the scanning tip.

We are grateful to Dr. S. Müller, Dr. B. Heymann, and L. Melanson for proofreading and discussing the manuscript. We thank Dr. Wolfgang Baumeister for the HPI layers, Dr. Georg Büldt for the purple membrane, Kenny Goldie for the amylin, Dr. Andreas Hoenger for the porin OmpF crystals, Dr. Wil Konings for the liposomes, Dr. José Maria Valpuesta for the ø29 connector crystals, and Dr. Georgios Tsiotis for the photosystem II complexes. D.J.M. is grateful to Dr. Georg Büldt for his continuous support. This work was supported by the Swiss National Foundation for Scientific Research (NFP 36, Grant 4036-044062 to A.E.), the Deutsche Forschungsgemeinschaft (SFB 189 to D.J.M.), and the Maurice E. Müller Foundation of Switzerland.

REFERENCES

Agre, P., Preston, G. M., Smith, B. L., Jung, J. S., Raina, S., Moon, C., Guggino, W. B., and Nielsen, S. (1993) Aquaporin CHIP: The archetypal molecular water channel, *Am. J. Physiol.* **265,** F463–F476.

Bailey, S. W. (1984) Micas, *Rev. Miner.* **13.**

Baumeister, W., Barth, M., Hegerl, R., Guckenberger, R., Hahn, M., and Saxton, W. O. (1986) Three-dimensional structure of the regular surface layer (HPI layer) of *Deinococcus radiodurans*, *J. Mol. Biol.* **187,** 241–253.

Baumeister, W., Karrenberg, F., Rachel, R., Engel, A., Ten Heggeler, B., and Saxton, W. O. (1982) The major cell envelope protein of *Micrococcus radiodurans* (R1), *Eur. J. Biochem.* **125,** 535–544.

Binnig, G., Quate, C. F., and Gerber, C. (1986) Atomic force microscope, *Phys. Rev. Lett.* **56,** 930–933.

Binnig, G., Rohrer, H., Gerber, C., and Weibel, E. (1982) Tunneling through a controllable vacuum gap, *Appl. Phys. Lett.* **40,** 178.

Butt, H.-J., Jaschke, M., and Ducker, W. (1995) Measuring surface forces in aqueous solution with the atomic force microscope, *Bioelect. Bioenerg.* **38,** 191–201.

Butt, H.-J., Siedle, P., Seifert, K., Fendler, K., Seeger, T., Bamberg, E., Weisenhorn, A. L., Goldie, K., and Engel, A. (1993) Scan speed limit in atomic force microscopy, *J. Microsc.* **169,** 75–84.

Butt, H.-J. (1992a) Electrostatic interaction in scanning probe microscopy when imaging in electrolyte solutions, *Nanotechnology* **3,** 60–68.

Butt, H.-J. (1992b) Measuring local surface charge densities in electrolyte solutions with an scanning force microscope, *Biophys. J.* **63,** 578–582.

Butt, H.-J., Guckenberger, R., and Rabe, J. P. (1992) Quantitative scanning tunneling microscopy and scanning force microscopy of organic materials, *Ultramicroscopy* **46,** 375–393.

Butt, H.-J., Prater, C. B., and Hansma, P. K. (1991) Imaging purple membranes dry and in water with the atomic force microscope, *J. Vac. Sci. Technol. B* **9**(2), 1193–1197.

Butt, H.-J. (1991) Electrostatic interaction in atomic force microscopy, *Biophys. J.* **60,** 777–785.

Butt, H.-J., Downing, K. H., and Hansma, P. K. (1990) Imaging the membrane protein bacteriorhodopsin with the atomic force microscope, *Biophys. J.* **58,** 1473–1480.

Carazo, J. M., Fujisawa, H., Nakasu, S., and Carrascosa, J. L. (1986) Bacteriophage T3 gene 8 product oligomer structure, *J. Ultrastruct. Mol. Struct. Res.* **94,** 105–113.

Carazo, J. M., Santisteban, A., and Carrascosa, J. L. (1985) Three-dimensional reconstruction of the bacteriophage Ø29 neck particles at 2.2 nm resolution, *J. Mol. Biol.* **183,** 79–88.

Carrascosa, J. L., Carazo, J. M., Herranz, L., Donate, L. E., and Secilla, J. P. (1990) Study of two related configurations of the neck of bacteriophage ø29, *Computers Math. Appl.* **20,** 57–65.

Carrascosa, J. L., Vinuela, E., Garcia, N., and Santisteban, A. (1982) Structure of the head-tail connector of bacteriophage ø29, *J. Mol. Biol.* **154,** 311–324.

Cerritelli, M. E., and Studier, W. (1996) Purification and character-

ization of T7 head-tail connectors expressed from the cloned gene, *J. Mol. Biol.* **258,** 299–307.

Cevc, G., and Marsh, D. (1985) Phospholipid Bilayers: Physical Principles and Models, Wiley, New York.

Cooper, G. S. (1994) Amylin compared with calcitonin gene-related peptide: Structure, biology, and relevance to metabolic disease, *Endocr. Rev.* **15,** 163–201.

Cowan, S. W., Schirmer, T., Rummel, G., Steiert, M., Ghosh, R., Pauptit, R. A., Jansonius, J. N., and Rosenbusch, J. P. (1992) Crystal structures explain functional properties of two *E. coli* porins, *Nature* **358,** 727–733.

Dencher, N. A., Dresselhaus, D., Zaccai, G., and Büldt, G. (1989) Structural changes in bacteriorhodopsin during proton translocation revealed by neutron diffraction, *Proc. Natl.-Acad. Sci. USA* **86,** 7876–7879.

Drake, B., Prater, C. B., Weisenhorn, A. L., Gould, S. A. C., Albrecht, T. R., Quate, C. F., Cannell, D. S., Hansma, H. G., and Hansma, P. K. (1989) Imaging crystals, polymers, and processes in water with the atomic force microscope, *Science* **243,** 1586–1588.

Driedonks, R. A., Engel, A., tenHeggeler, B., and van Driel, R. (1981) Gene 20 product of bacteriophage T4 its purification and structure, *J. Mol. Biol.* **152,** 641–662.

Dube, P., Tavares, P., Lurz, R., and van Heel, M. (1993) The portal protein of bacteriophage SPP1: A DNA pump with 13-fold symmetry, *EMBO J.* **12,** 1303–1309.

Elferink, M. G. L., de Wit, J. G., Driessen, A. J. M., and Konings, W. N. (1994) Stability and proton-permeability of liposomes composed of archaeal tetraether lipids, *Biochim. Biophys. Acta* **1193,** 247–254.

Elferink, M. G. L., de Wit, J. G., Driessen, A. J. M., and Konings, W. N. (1993) Energy-transducting properties of primary proton pumps reconstituted into archaeal bipola lipid vesicles, *Eur. J. Biochem.* **214,** 917–925.

Elferink, M. G. L., de Wit, J. G., Demel, R., Driessen, A. J. M., and Konings, W. N. (1992) Functional reconstitution of membrane proteins in monolayer liposomes from bipolar lipids in *Sulfolobus acidocaldarius*, *J. Biol. Chem.* **2647,** 1375–1381.

Engel, A., Schoenenberger, C.-A., and Müller, D. J. (1997) High-resolution imaging of native biological sample surfaces with scanning probe microscope, *Curr. Opin. Struct. Biol.* **7,** 279–284.

Engel, A., Baumeister, W., and Saxton, W. (1982) Mass mapping of a protein complex with the scanning transmission electron microscope, *Proc. Natl. Acad. Sci. USA* **79,** 4050–4054.

Fritz, M., Radmacher, M., Allersma, M. W., Cleveland, J. P., Stewart, R. J., Hansma, P. K., and Schmidt, C. F. (1995a) Imaging microtubles in buffer solution using tapping mode atomic force microscopy, *SPIE* **2384,** 150–157.

Fritz, M., Radmacher, M., Cleveland, J. P., Allersma, M. W., Steward, R. J., Gieselmann, R., Janmey, P., Schmidt, C. F., and Hansma, P. K. (1995b) Imaging globular and filamentous proteins in physiological buffer solutions with tapping mode atomic force microscopy, *Langmuir* **11,** 3529–3535.

Gaines, G., and Tabor, D. (1956) Surface adhesion and elastic properties of mica, *Nature* **178,** 1304–1305.

Goldsbury, C. S., Cooper, G. J. S., Goldie, K. N., Müller, S. A., Saafi, E. L., Guijters, W. T. M., Misur, M. P., Engel, A., and Aebi, U. (1996) The human amylin protofilament: Unitary structure underlying the polymorphism of complex fibrillar assemblies. *J. Struct. Biol,* in press.

Grigorieff, N., Ceska, T. A., Downing, K. H., Baldwin, J. M., and Henderson, R. (1996) Electron-crystallographic refinement of the structure of bacteriorhodopsin, *J. Mol. Biol.* **259,** 393–421.

Haltia, T., and Freire, E. (1995) Forces and factors that contribute to the structural stability of membrane proteins, *Bba-Bioenergetics* **1228,** 1–27.

Hansma, H. G., and Laney, D. E. (1996) DNA binding to mica correlates with cationic radius: Assay by atomic force microscopy, *Biophys. J.* **70,** 1933–1939.

Hansma, H. G., Laney, D. E., Bezanilla, M., Sinsheimer, R. L., and Hansma, P. K. (1995) Applications for atomic force microscopy of DNA, *Biophys. J.* **68,** 1672–1677.

Hansma, H. G., Vesenka, J., Siegerist, C., Kelderman, G., Morrett, H., Sinsheimer, R. L., Elings, V., Bustamate, C., and Hansma, P. K. (1992) Reproducible imaging and dissection of plasmid DNA under liquid with the atomic force microscope, *Science* **256,** 1180–1184.

Hasler, L., Ghanotakis, D., Fedtke, B., Spyridaki, A., Miller, M., Müller, S. A., Engel, A., and Tsiotis, G. (1997) Structural analysis of photosystem II: comparative study of cyanobacterial and higher plant photosystem II complexes. *J. Struct Biol,* in press.

Hegner, M., Dreier, M., Wagner, P., Semenza, G., and Güntherodt, H.-J. (1996) Modified DNA immobilized on bioreactive self-assembled monolayer on gold for dynamic force microscopy imaging in aqueous buffer solution, *J. Vac. Sci. Technol. B* **14,** 1418–1421.

Hegner, M., Wagner, P., and Semenza, G. (1993) Immobilizing DNA on gold via thiol modification for atomic force microscopy imaging in buffer solutions, *FEBS Lett.* **336,** 452–456.

Henderson, R., Baldwin, J. M., Ceska, T. A., Zemlin, F., Beckman, E., and Downing, K. H. (1990) Model for the structure of bacteriorhodopsin based on high-resolution electron cryo-microscopy, *J. Mol. Biol.* **213,** 899–929.

Hoenger, A., Ghosh, R., Schoenenberger, C.-A., Aebi, U., and Engel, A. (1993) Direct *in situ* structural analysis of recombinant outer membrane proteins expressed in an OmpA-deficient mutant *Escherichia coli* strain, *J. Struct. Biol.* **111,** 212–221.

Hoh, J. H., Sosinsky, G. E., Revel, J.-P., and Hansma, P. K. (1993) Structure of the extracellular surface of the gap junction by atomic force microscopy, *Biophys. J.* **65,** 149–163.

Ibañez, C., García, J. A., Carrascosa, J. L., and Salas, M. (1984) Overproduction and purification of the connector protein of *Bacillus subtilis, Nucleic Acids Res.* **12,** 2351–2365.

Israelachvili, J. (1991) Intermolecular and Surface Forces, Academic Press, London.

Jap, B. K., Zulauf, M., Scheybani, T., Hefti, A., Baumeister, W., Aebi, U., and Engel, A. (1992) 2D crystallization: from art to science, *Ultramicroscopy* **46,** 45–84.

Jubb, J. S., Worcester, D. L., Crespi, H. L., and Zaccai, G. (1984) Retinal location in purple membrane of *Halobacterium halobium:* A neutron diffraction study of membranes labeled *in vivo* with deuterated retinal, *EMBO J.* **3,** 1455–1461.

Karrasch, S., Hegerl, R., Hoh, J., Baumeister, W., and Engel, A. (1994) Atomic force microscopy produces faithful high-resolution images of protein surfaces in an aqueous environment, *Proc. Natl. Acad. Sci. USA* **91,** 836–838.

Karrasch, S., Dolder, M., Hoh, J., Schabert, F., Ramsden, J., and Engel, A. (1993) Covalent binding of biological samples to solid supports for scanning probe microscopy in buffer solution, *Biophys. J.* **65,** 2437–2446.

Kates, M., Kushawa, S. C., and Sprott, G. D. (1982) Lipids of purple membrane from extreme halophiles and of methanogenic bacteria, *Methods Enzymol.* **88,** 98–111.

Kochan, J., Carrascosa, J. L., and Murialdo, H. (1984) Bacteriophage lambda preconnectors. Purification and structure, *J. Mol. Biol.* **174,** 433–447.

Kocsis, E., Cerritelli, M., Trus, B., Cheng, N., and Steven, A. C.

(1995) Improved methods for determination of rotational symmetries in macromolecules, *Ultramicroscopy* **60,** 219–228.

Lakey, J. H. (1987) Voltage gating in porin channels, *FEBS Lett.* **211,** 1–4.

Lanyi, J. K. (1993) Proton translocation mechanism and energetics in the light-driven pump bacteriorhodopsin, *Biochem. Biophys. Acta* **1183,** 241–261.

McLaughlin, S. (1989) The electrostatic properties of membranes, *Annu. Rev. Biophys. Chem.* **18,** 113–136.

Mishra, R. K., and Ghanotakis, D. F. (1994) Selective extraction of CP 26 and CP 29 proteins without affecting the binding of the extrinsic proteins (33, 23 and 17 kDa) and the DCMU sensitivity of a Photosystem II core complex, *Photosyn. Res.* **42,** 37–42.

Mou, J., Czajkowsky, D. M., Sheng, S., Ho, R., and Shao, Z. (1996) High resolution surface structure of *E. coli* GroES oligomer by atomic force microscopy, *FEBS Lett.* **381,** 161–164.

Müller, D. J., Engel, A., Carrascosa, J., and Veléz, M. (1997a) The bacteriophage ø29 head-tail connector imaged at high resolution with atomic force microscopy in buffer solution, *EMBO J.* **16,** 2547–2553.

Müller, D. J., Schoenenberger, C.-A., Schabert, F., and Engel, A. (1997b) Structural changes of native membrane proteins monitored at subnanometer resolution with the AFM, *J. Struct. Biol.,* in press.

Müller, D. J., and Engel, A. (1997c) The height of biomolecules measured with the atomic force microscope depends on electrostatic interactions. *Biophys. J.*, in press.

Müller, D. J., Baumeister, W., and Engel, A. (1996a) Conformational change of the hexagonally packed intermediate layer imaged by atomic force microscopy, *J. Bacteriol.* **178,** 3025–3030.

Müller, D. J., Schoenenberger, C. A., Büldt, G., and Engel, A. (1996b) Immuno-atomic force microscopy of purple membrane, *Biophys. J.* **70,** 1796–1802.

Müller, D. J., Büldt, G., and Engel, A. (1995a) Force-induced conformational change of bacteriorhodopsin, *J. Mol. Biol.* **249,** 239–243.

Müller, D. J., Schabert, F. A., Büldt, G., and Engel, A. (1995b) Imaging purple membranes in aqueous solutions at subnanometer resolution by atomic force microscopy. *Biophys. J.* **68,** 1681–1686.

Oesterhelt, D., and Stoeckenius, W. (1974) Isolation of the cell membrane of *Halobacterium halobium* and its fraction into red and purple membrane, *Methods Enzymol.* **31,** 667–678.

Pashley, R. M. (1981) Hydration forces between mica surfaces in Li^+, Na^+, Na^+ and Cs^+ electrolyte solutions: A correlation of double layer and hydration forces with surface cation exchange properties, *J. Colloid Interface Sci.* **83,** 531–546.

Peters, J., Peters, M., Lottspeich, F., Schäfer, W., and Baumeister, W. (1987) Nucleotide sequence of the gene encoding the *Deinococcus radiodurans* surface protein, derived amino acid sequence, and complementary protein chemical studies, *J. Bacteriol.* **169,** 5216–5223.

Pittner, R. A., Albrandt, K., Beaumont, K., Gaeta, L. S., Koda, J. E., Moore, C. X., Rittenhouse, J., and Rink, T. J. (1994) Molecular physiology of amylin, *J. Cell. Biochem.* **55,** 19–28.

Ross, P. E., Helgerson, S. L., Miercke, L. J. W., and Dratz, E. A. (1989) Isoelectric focusing studies of bacteriorhodopsin, *Biochim. Biophys. Acta* **991,** 134–140.

Schabert, F. A., Henn, C., and Engel, A. (1995) Native *Escherichia coli* OmpF porin surfaces probed by atomic force microscopy, *Science* **268,** 92–94.

Schabert, F., Hoh, J. H., Karrasch, S., Hefti, A., and Engel, A. (1994) Scanning force microscopy of *E. coli* OmpF porin in buffer solution, *J. Vac. Sci. Technol. B.* **12,** 1504–1507.

Schabert, F. A., and Engel, A. (1994) Reproducible acquisition of *Escherichia coli* porin surface topographs by atomic force microscopy, *Biophys. J.* **67,** 2394–2403.

Shao, Z., Mou, J., Czajkowsky, D. M., Yang, J., and Yuan, J.-Y. (1996) Biological atomic force microscopy: what is achieved and what is needed, *Adv. Phys.* **45,** 1–86.

Smith, B. L., and Agre, P. (1991) Erythrocyte Mr 28,000 transmembrane protein exists as a multisubunit oligomer similar to channel proteins, *J. Biol. Chem.* **266,** 6407–6415.

Steinhoff, H.-J., Mollaaghababa, R., Altenbach, C., Hideg, K., Khorana, H. G., and Hubbell, W. L. (1994) Time-resolved detection of structural changes during the photocycle of spin-labeled bacteriorhodopsin, *Science* **266,** 105–107.

Steinhoff, H.-J., Mollaaghababa, R., Altenbach, C., Khorana, H. G., and Hubbell, W. L. (1995) Site directed spin labeling studies of structure and dynamics in bacteriorhodopsin, *Biophys. Chem.* **56,** 89–94.

Subramaniam, S., Gerstein, M., Oesterhelt, D., and Henderson, R. (1993) Electron diffraction analysis of structural changes in the photocycle of bacteriorhodopsin, *EMBO J.* **12,** 1–8.

Todt, J. C., Rocque, W. J., and McGroarty, E. J. (1992) Effects of pH on bacterial porin function, *Biochemistry* **31,** 10471–10478.

Tsiotis, G., Walz, T., Spyridaki, A., Lustig, A., Engel, A., and Ghanotakis, D. (1996) Tubular cristals of a photosystem II core complex, *J. Mol. Biol.* **259,** 241–248.

Tsuprun, V., Anderson, D., and Egelman, E. H. (1994) The bacteriophage ø29 head-tail connector shows 13-fold symmetry in both hexagonally packed arrays and as single particles, *Biophys. J.* **66,** 2139–2150.

Valpuesta, J. M., and Carrascosa, J. L. (1994) Structure of viral connectors and their function in bacteriophage assembly and DNA packaging, *Q. Rev. Biophys.* **27,** 107–155.

Valpuesta, J. M., Carrascosa, J. L., and Henderson, R. (1994) Analysis of electron microscope images and electron diffraction patterns of thin crystals of ø29 connectors in ice, *J. Mol. Biol.* **240,** 281–287.

Vikholm, I., Peltonen, J., and Teleman, O. (1995) Atomic force microscope images of lipid layers spread from vesicle suspensions, *Bba-Biomembranes* **1233,** 111–117.

Wagner, P., Hegner, M., Güntherodt, H.-J., and Semenza, G. (1995) Formation and *in situ* modification of monolayers chemisorbed on ultraflat template-stripped gold surfaces, *Langmuir* **11,** 3867–3875.

Wagner, P., Kernen, P., Hegner, M., Ungewickell, E., and Semenza, G. (1994) Covalent anchoring of proteins onto gold-directed NHS-terminated self-assembled monolayers in aqueous buffers: SFM images of clathrin cages and triskelia, *FEBS Lett* **356,** 267–271.

Walz, T., Tittmann, P., Fuchs, K. H., Müller, D. J., Smith, B. L., Agre, P., Gross, H., and Engel, A. (1996) Surface topographies at subnanometer-resolution reveal asymetry and sidedness of aquaporin-1, *J. Mol. Biol.* **264,** 907–918.

Walz, T., Smith, B. L., Agre, P., and Engel, A. (1994) The three-dimensional structure of human erythrocyte aquaporin chip, *EMBO J.* **13,** 2985–2993.

Walz, T., Smith, B. L., Zeidel, M. L., Engel, A., and Agre, P. (1994) Biologically active two-dimensional crystals of aquaporin CHIP, *J. Biol. Chem.* **269,** 1583–1586.

Weisenhorn, A. L., Khorsandi, M., Kasas, S., Gotzos, V., and Butt, H.-J. (1993) Deformation and height anomaly of soft surfaces studied with an AFM, *Nanotechnology* **4,** 106–113.

Wilson, J. A., and Yoffe, A. D. (1969) The transition metal dichalcogenides discussion and interpretation of the observed optical, electrical and structural properties, *Adv. Phys.* **18,** 193–335.